

UNIVERSITÄT TÜBINGEN

MASTER THESIS

LOOKING INTO THE ACCRETION
STRUCTURE OF
VELA X-1

Robert McCULLOCH

Römerhofweg 20

72108 Rottenburg am Neckar

mcculloch@astro.uni-tuebingen.de

October 2021

Eidesstattliche Erklärung

Hiermit versichere ich, dass ich gemäß des allgemeinen Teils der Studien- und Prüfungsordnung der Universität Tübingen für den Studiengang Physik mit akademischer Abschlussprüfung Master of Science (M.Sc.) vom DATE diese Masterarbeit mit dem Titel “TITLE” selbstständig verfasst und keine anderen als die angegebenen Hilfsmittel und Quellen benutzt habe. Alle wörtlich oder sinngemäß aus anderen Werken übernommenen Aussagen wurden als solche kenntlich gemacht. Die Arbeit war weder vollständig noch in wesentlichen Teilen Gegenstand eines anderen Prüfungsverfahrens und wurde weder vollständig noch in wesentlichen Teilen bereits veröffentlicht.

Ort, Datum

Unterschrift

Abstract

In this thesis, the X-ray binary system Vela X-1 was investigated using data from both the European Photon Imaging Camera (EPIC) and the Reflection Grating Spectrometer (RGS) detectors on board the XMM-Newton satellite. Light curves were generated showing the possible detection of a flare. New insight into the spectral model of the high mass X-ray binary system was found and potentially a new understanding for the model interpretation. An echo was confirmed to exist in the extended stellar wind of the companion star, as well as the firm detection of highly ionised elements and Radiation Recombination Continua (RRC), indicating the ionisation state of the plasma. Furthermore the line velocities were shown to be consistent with zero. Further analysis is required for this work and will be available in the paper that will be published in the near future.

Contents

List of Figures	ix
List of Tables	xi
1 Astrophysical Background	1
1.1 Introduction	1
1.2 Units	1
1.3 Compact Objects	2
1.4 Neutron Stars	2
1.4.1 Pulsars	3
1.5 X-ray Binaries	4
1.5.1 High Mass X-ray Binaries	4
1.5.2 Low Mass X-ray Binaries	5
1.6 Accretion	6
1.6.1 Stellar Wind	8
1.7 Vela X-1	9
1.8 Spectral Features	10
1.9 Doppler Effect	15
2 X-ray Multi Mirror Mission	17
2.1 XMM-Newton	17
2.2 Wolter Type-1 X-ray Telescope	17
2.3 Detectors	19
2.3.1 European Photon Imaging Camera	19
2.3.2 Reflection Grating Spectrometers	20
3 Data Reduction & Processing	23
3.1 EPIC	23
3.1.1 Pile-up	23
3.1.2 Response Files	26
3.1.3 Light Curves	27

3.2	RGS	27
3.2.1	Light Curve Extraction Issue	29
4	Data Analysis & Results	31
4.1	EPIC	31
4.1.1	Light Curves	31
4.1.2	Hardness Ratios	33
4.1.3	Previous Modelling Efforts	35
4.2	Chi-Square	37
4.2.1	Hard Spectrum	38
4.2.2	Total Spectrum	41
4.3	RGS1	43
4.3.1	Light Curve	43
4.4	Cash Statistics	44
4.4.1	High-resolution spectroscopy	45
4.4.2	Continuum Model	45
4.4.3	Absorbed Power Law	45
4.4.4	Narrow Band Spectral features	46
4.4.5	Radiative recombination continua	49
4.4.6	Best Fit model	49
4.4.7	Model Comparison	50
4.4.8	Line Velocities	51
5	Discussion	53
5.1	Light Curves	53
5.2	Accretion structure	53
5.3	Narrow-band Spectral Features	55
5.4	R and G diagnostic	56
6	Conclusion	59
	Title Appendix	61
	Bibliography	63

List of Figures

1.1	The internal structure of a $1.4 M_{\odot}$ NS (Longair 2011)	3
1.2	Schematic view for the different types of X-ray binaries (Courvoisier 2013)	5
1.3	Left: The equipotential surfaces of a binary star system in the rotating frame of reference. Right: The star fills its Roche lobe and matter passes through the Lagrangian point L_1 onto the compact object and an accretion disc is formed (Longair 2011)	6
1.4	Different geometries of the accretion column. (a) Filled funnel (b) Hollow funnel (c) Pancake (d) Spaghetti (Mészáros 1984)	7
1.5	Left: Fan beam. Right: Pencil beam (Schönherr et al. 2007)	8
1.6	Illustration of a compact object deeply embedded in the stellar wind of a massive star (Longair 2011)	9
1.7	Schematic diagram of the different transition series (Santangelo & Grinberg 2021)	13
1.8	Schematic diagram of energy levels for He-like ions (ASTRO-H Cookbook Members 2015)	14
2.1	Sketch of the XMM-Newton (ESA: XMM-Newton SOC 2019)	18
2.2	The light path and assembly of the Wolter type-1 X-ray telescope (ESA: XMM-Newton SOC 2019)	18
2.3	The light path of the other two X-ray telescope. Note the actual portion of light that is directed to the main focus is 44% (ESA: XMM-Newton SOC 2019)	19
2.4	Layout comparison in the focal plane of the EPIC MOS and pn cameras (ESA: XMM-Newton SOC 2019)	20
2.5	RGS MOS CCD bench arrangement (den Herder et al. 2000)	21
3.1	Left: Distribution of Counts vs PI channel for each pattern Class. Right: Expected pattern distribution plotted with Observed distribution. The top to bottom panel show the first, second and third iterations respectively	25
3.2	RGS 1 - Top: The Cross Dispersion Angle vs Wavelength. Bottom: PI channel vs Wavelength	28

3.3	RGS 2 - Top: The Cross Dispersion Angle vs Wavelength. Bottom: PI channel vs Wavelength	29
4.1	EPIC Light Curve. Note that the error bars are smaller than the data points	32
4.2	Light Curve of multiple bands. Note that the error bars are smaller than the data points	33
4.3	Light Curve of multiple bands with log scaled count rates. Note that the error bars are smaller than the data points	34
4.4	Two numerical solutions	36
4.5	Spectrum 15 from Martínez-Núñez et al. (2014)	37
4.6	Spectral data (2.6- 10 keV)	38
4.7	Hard Spectrum (2.6- 10 keV)	40
4.8	Total Spectrum (0.6- 10 keV)	43
4.9	Light Curve of RGS 1	44
4.10	Two numerical solutions	47
4.11	RGS	48
4.12	RGS 1 Best fit model	50
4.13	RGS 1 Best fit model	51
5.1	Schematic view of the physical interpretation	55
1	Two pixel columns either side of the boresight	61
2	Groupings	62

List of Tables

2.1	Overview of XMM-Newton instruments (ESA: XMM-Newton SOC 2019)	21
4.1	Expected element regions	42
4.2	Detected emission lines for RGS 1 spectrum	49
4.3	Line Velocities	52

Astrophysical Background

1.1 Introduction

Vela X-1 is one of the most studied X-ray binaries in astronomy and has been observed by every major X-ray instrument (Kretschmar et al. 2019). This is mainly because the source is an early discovery, which was made by Chodil et al. (1967). It is located at the following coordinates: Right ascension of 09 h 02' 06.86" and declination of $-40^{\circ} 33' 16.9''$ (HEASARC 2021). The X-ray emission from the system was observed to have brightness variations by Forman et al. (1973), where eclipses were found to be the cause (Ulmer et al. 1972). Vela X-1 is now known as one of the brightest sources in the X-ray sky with persistent X-ray emission that has irregular flux variations. In comparison to other X-ray binary systems, the parameters for Vela X-1 are well known, making it possible to do model comparisons with data in more detail (Kretschmar et al. 2019). It is regarded as an ideal model for wind-accreting high-mass X-ray binaries. In this thesis the accretion structure of Vela X-1 is investigated.

1.2 Units

The physical quantities are given in the centimeter-gram-second (cgs) system of units. Sometimes the units are not expressed in cgs, but if the reader wishes to convert from alternate units, these are the necessary conversions needed for this thesis. Energies are given in keV, where $1 \text{ keV} \approx 1.6 \times 10^9 \text{ erg}$. Power is given in watts, where $1 \text{ W} = 1 \times 10^7 \text{ erg/s}$. $1 \text{ km} = 100000 \text{ cm}$. $1 \text{ kg m}^{-3} = 0.001 \text{ g cm}^{-3}$. Angstrom $1 \text{ \AA} = 1 \times 10^{-8} \text{ cm}$. The energy range of X-ray radiation in the electromagnetic spectrum is from 0.1 to 100 keV (Longair 2011). Distances are given in kpc, where $1 \text{ kpc} \approx 3.1 \times 10^{21} \text{ cm}$. Masses and radii are in units of solar mass (M_{\odot}) and solar radii (R_{\odot}). Here $1 M_{\odot} \approx 1.99 \times 10^{33} \text{ g}$ and $1 R_{\odot} \approx 6.96 \times 10^{10} \text{ cm}$.

1.3 Compact Objects

Stars are stabilised by thermal pressure of hot gas being in balance with gravity. The source of energy for thermal pressure is nuclear fusion, which occurs in the stars inner core. As the star shifts from the main sequence, up the giant branch and towards the final phases of its evolution, the available nuclear energy is eventually exhausted. The more mass the star has, the faster it will evolve. At the end of the stars life, the outer layers will be ejected and the core will collapse until another form of pressure support enables a new equilibrium configuration to be reached. Possible equilibrium configurations are white dwarfs, Neutron Stars (NSs) or black holes, which are known as compact objects. White dwarfs and NSs, are supported by a degeneracy pressure which is related to the Pauli exclusion principle, which states that only one fermion can occupy a single quantum state in a system. White dwarfs are stabilised by the electron degeneracy pressure and can have masses up to about $1.4 M_{\odot}$ (Longair 2011), where as NSs are stabilised by the neutron degeneracy pressure and are thought to have a mass range between $1.4 M_{\odot} < M_{NS} < 2.0 M_{\odot}$ (Santangelo & Grinberg 2021). Compact objects with mass greater than $2.5 M_{\odot}$ are black holes (Longair 2011). The compact object that this research is related to is the NS, which will be the focus of the following section (Longair 2011).

1.4 Neutron Stars

NSs typically have a radius that ranges from 10 – 14km and a mass that ranges from $1.4 - 2.0 M_{\odot}$. This makes them extremely dense objects with a mean density of $7 \times 10^{14} \text{ g cm}^{-3}$, which is on the same order of magnitude for nuclear densities (Santangelo & Grinberg 2021). They also have intense magnetic fields that range from $10^9 - 10^{15} \text{ G}$ (Santangelo & Grinberg 2021). NSs are composed almost entirely of neutrons where the interior has zones of increasing density below the surface. The internal structure is not well defined due to uncertainties in the equation of state (EOS), which is the relationship between pressure and density. For the NS the EOS describes the degenerate nuclear matter in the interior (Longair 2011). Figure 1.1 shows a possible model of the NSs internal structure. The various regions are described below:

- The surface layer has density on the order of 10^9 kg m^{-3} , which consists of a close packed solid made up of ^{56}Fe .
- The outer crust has density in the range of $10^9 - 4.3 \times 10^{14} \text{ kg m}^{-3}$ and consists of a solid region composed of a heavy nuclei forming a Coulomb lattice embedded

in a relativistic electron degenerate gas.

- The inner crust has density between $4.3 \times 10^{14} - 2 \times 10^{17} \text{ kg m}^{-3}$. This region consists of a lattice of neutron-rich nuclei, free degenerate neutrons and a relativistic electron degenerate gas. At such densities, nuclei start to dissolve forming a neutron super fluid.
- Further into the interior, the density is greater than $2 \times 10^{17} \text{ kg m}^{-3}$. This region is made up of the neutron super fluid with a small concentration of protons and electrons.
- At the core of the NS, the phase of matter is unknown. It is thought that in this region $\rho \geq 3 \times 10^{18} \text{ kg m}^{-3}$ and exotic forms of matter could exist, such as condensate, neutron solid or quark matter.

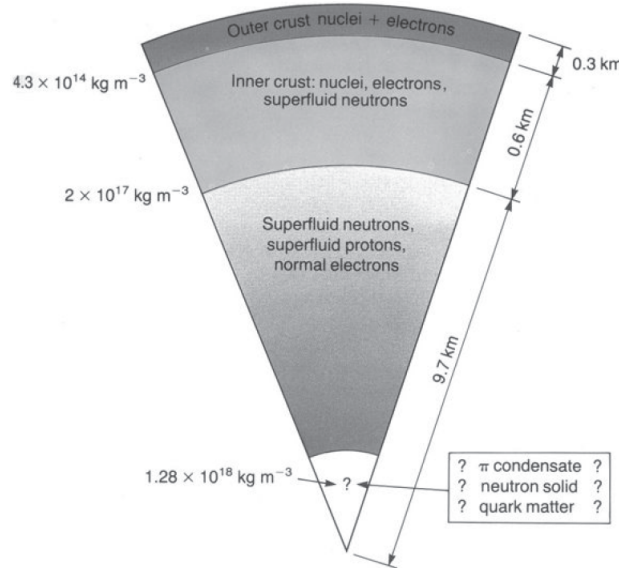


Figure 1.1: The internal structure of a $1.4 M_{\odot}$ NS (Longair 2011)

1.4.1 Pulsars

When a massive star collapses into a NS it has an initial angular momentum, which is dependent on the radius squared. Since the NS radius is much smaller than the initial radius of the core, when the collapse is complete, the rotational speed of the newly formed NS will vastly increase. They can reach rotational periods on the order of milliseconds, which is a direct result from the conservation of angular momentum. Near the magnetic poles of the rotating NS, beams are produced by streams of charged particles moving along the NSs magnetic field lines, emitting electromagnetic radiation

in the process. If the rotating beams radiated from the poles intercept our field of view, we observe them as pulses, that come from a fixed point in the sky. These rotating NSs are known as Pulsars (Santangelo & Grinberg 2021).

1.5 X-ray Binaries

There are a number of different X-ray sources in the Milky Way Galaxy that are generated through different physical processes. A portion of these sources are made up of X-ray binaries (XRBs), which are systems that consist of a compact object and a companion star. Since these systems have varied properties they are classified into different categories. Figure 1.2 shows a schematic view of the different types. If the compact object is a white dwarf, then the system is defined as a cataclysmic variable. In this case material is pulled onto the surface of the white dwarf from the companion star. As more matter accumulates onto the surface, its mass increases eventually exceeding the Chandrasekhar limit and consequently leading to a type I supernova (Courvoisier 2013). Since this particular binary system is not relevant to this research, it is no longer discussed. Further distinction in the classification is dependant on the mass of the companion star M_* . If $M_* > 10 M_\odot$ then this is categorised as a high mass X-ray binary (HMXRB) system, where as if $M_* < M_\odot$ it is classified as a low mass X-ray binary (LMXRB) system (Casares et al. 2017). A final distinction is related to the mass of the compact object. If the mass is greater than $3M_\odot$ then the system consists of a black hole candidate, otherwise in the other case it will contain a NS. The main focus of this work will be dealing with a HMXRB system that consists of a NS. Nevertheless, in the following section, I will elaborate on both high and low mass X-ray binaries (Courvoisier 2013).

1.5.1 High Mass X-ray Binaries

HMXRBs are systems that typically consist of O or B type companion stars, which are stars greater than $10 M_\odot$, and are in orbit with a compact object. The X-ray emission from such a system is dominated by the emission of optical light, which make these systems relatively easy to detect. Since HMXRBs are young systems they are generally found in the star formation regions in the disk of our galaxy. These particular systems usually undergo wind accretion, which will be discussed in further detail in a later section, where the compact object is embedded in the stellar wind of the companion star (Courvoisier 2013).

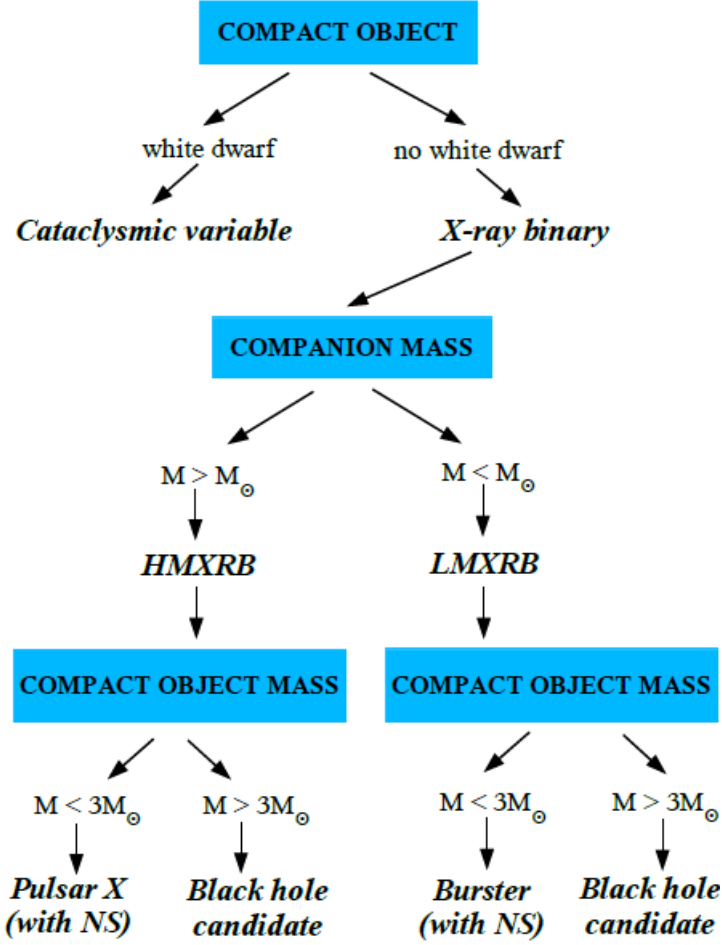


Figure 1.2: Schematic view for the different types of X-ray binaries (Courvoisier 2013)

1.5.2 Low Mass X-ray Binaries

When the companion star of XRBs is less than or on the order of the mass of the sun, then it is labelled a LMXRB system. In this case the X-ray luminosity is much larger than the optical luminosity. Since low mass stars live longer than massive stars, LMXRBs are usually old systems and are more concentrated in the bulge towards the center of our galaxy. In these systems accretion usually occurs through Roche lobe overflow (Courvoisier 2013). The left image in figure 1.3 shows the equipotential surfaces of a binary system in the rotating frame of reference. The critical equipotential surface that encloses both stars is the Roche lobe and is shown by the dashed line. Due to the expansion of the companion star, matter will start filling the Roche lobe and eventually overflow and pass through the inner Lagrangian point L_1 . Due to the conservation of angular momentum, this will result in the formation of an accretion disk around the compact object, which is shown in the right image in figure 1.3. Since this research is based on a HMXRB system that consists of a pulsar, LMXRBs and

Roche lobe overflow are no longer discussed. For more detail see (Longair 2011).

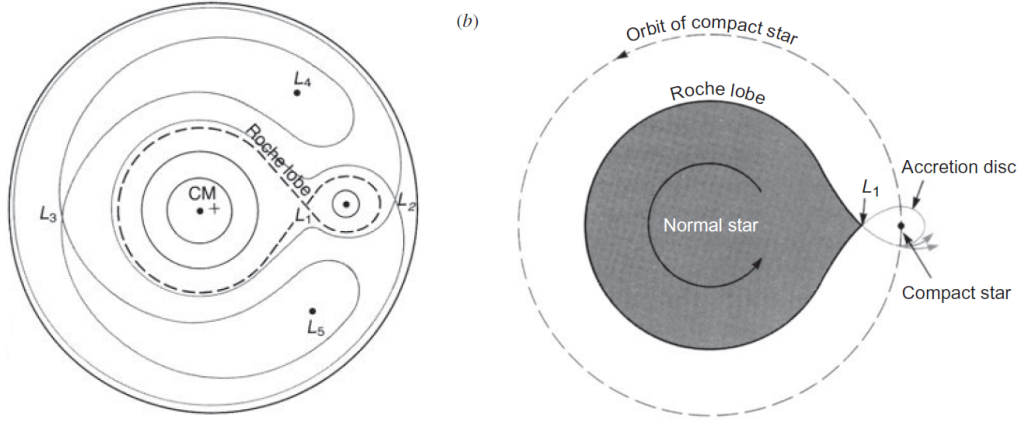


Figure 1.3: Left: The equipotential surfaces of a binary star system in the rotating frame of reference. Right: The star fills its Roche lobe and matter passes through the Lagrangian point L_1 onto the compact object and an accretion disc is formed (Longair 2011)

1.6 Accretion

Accretion is the accumulation of matter onto an object through the influence of gravity. It is the most efficient procedure in the universe by which rest mass energy is converted to heat. The luminosity generated by accretion is given by:

$$L_{acc} = \frac{GM\dot{m}}{R} \quad (1.1)$$

Where M and R are both the mass and radius of the compact object respectively, G the gravitational constant and \dot{m} is the rate at which mass is being accreted (Longair 2011). The luminosity of such systems has a limit, because if the luminosity were too large, the radiation pressure would push incoming matter away. This limit is known as the Eddington limit and is given by the following equation 1.2 (Longair 2011):

$$L_{Edd} = \frac{4\pi GMm_p c}{\sigma_T} = 1.3 \times 10^{38} \left(\frac{M}{M_\odot} \right) \text{ erg/s} \quad (1.2)$$

Where m_p is the proton mass, σ_T the Thomson cross section and c the speed of light. In the case of accreting NSs, which typically have strong magnetic fields, an additional component of complexity is introduced. Close to the NS, the magnetic field begins to dominate and therefore influences the way matter is transferred. In this process ionized

matter is coupled to the magnetic field lines and channelled towards the magnetic poles where an accretion column is formed. Since the details of how matter couples to the field lines is not really understood, it is not clear whether the accretion column is filled, hollow or has a pancake or spaghetti like structure, see figure 1.4.

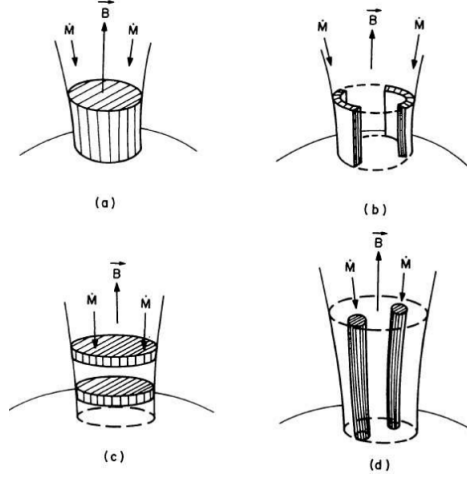


Figure 1.4: Different geometries of the accretion column. (a) Filled funnel (b) Hollow funnel (c) Pancake (d) Spaghetti (Mészáros 1984)

Closer to the NS poles, the structure of the emitting region at different luminosities can take on two different structures. For large accretion rates above the critical luminosity, which has a value around 1×10^{37} erg/s, a shock front will develop at some distance from the NS surface. This prevents the photons from escaping vertically from the accretion column. As a result X-rays are emitted to the side of the beam, where a “fan beam” emission pattern is formed, see left image of figure 1.5.

For low accretion rates below the critical luminosity, incoming matter is decelerated through the scattering of electrons in the NS atmosphere. Photons can therefore escape parallel to the B-field forming a “pencil beam” pattern (Basko & Syun'yayev 1976; Becker et al. 2012), see right image of figure 1.5.

The emitted X-ray spectrum of the column is complex where a key component is played by Compton scattering of thermal seed photons (Kretschmar et al. 2021). This is the process by which most of the X-ray emission we observe is thought to be generated, however, there is no current self-consistent physics that can correctly describe the spectra of accreting X-ray pulsars (Kretschmar et al. 2021).

The radius where the plasma flow is threaded by the magnetic field is known as the Alfvén radius R_A , which is determined from the balance between accreting plasma pressure and magnetic pressure (Kretschmar et al. 2019):

$$R_A = \left(\frac{\mu^2}{\dot{m}\sqrt{2GM}} \right)^{2/7} \quad (1.3)$$

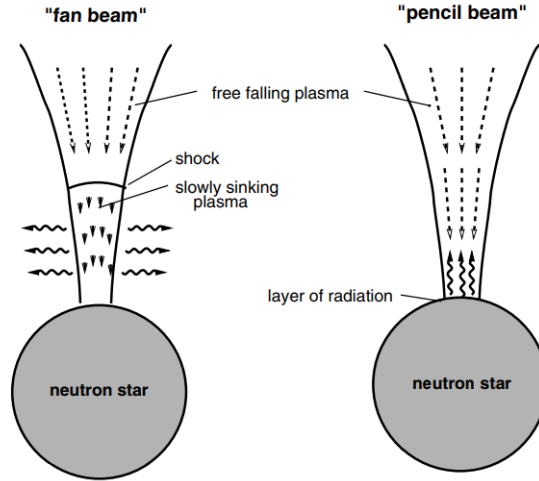


Figure 1.5: Left: Fan beam. Right: Pencil beam (Schönherr et al. 2007)

Here μ is the dipole magnetic moment and \dot{m} the mass accretion rate.

The boundary by which charged particles are affected by the magnetic field is located at a distance R_m from the NS. This is known as the magnetosphere boundary, which is dependant on R_A . There are two different forms of accretion that can occur here, either quasi-spherical or disc accretion. The type of accretion is determined by the specific angular momentum at R_m . A disc is formed if the angular momentum of the captured material is greater than the Keplerian value at the magnetosphere boundary, otherwise the system will undergo quasi spherical accretion. In the following section I will discuss accretion from wind-fed systems (Kretschmar et al. 2019).

1.6.1 Stellar Wind

Stellar wind can be characterised by two parameters. First the mass loss rate:

$$\dot{m} = 4\pi r^2 \rho(r) \nu(r) \quad (1.4)$$

Where r is the distance from the center of the star. Here $\rho(r)$ and $\nu(r)$ are both the density and velocity at distance r . Second we have the terminal velocity:

$$\nu_\infty = \frac{\nu(r)}{(1 - R_*/r)^\beta} \quad (1.5)$$

Where R_* is the stellar radius and β is the steepness of the wind velocity profile. The

acceleration of the wind is dependent on the following three conditions: ionisation, excitation and chemical composition. All stars eject radiatively driven stellar winds, however smaller stars like the sun experience inactive periods, whereas O and B type stars are more violent with mass loss rates reaching up to $10^{-6} M_{\odot} \text{ yr}^{-1}$ (Kretschmar et al. 2019). For HMXRBs, if the orbital distance of the compact object from the companion star is small, it will be embedded in the stellar wind of the companion as seen in figure 1.6. The compact object can influence the wind, and form a trailing accretion wake through gravitational focusing. The movement of the companion star can also create an accretion bow shock upstream of the compact object. X-ray emission in the system can then ionise the material in the local environment leading to the formation of a photoionisation wake, a plasma of ionised material (Blondin et al. 1990).

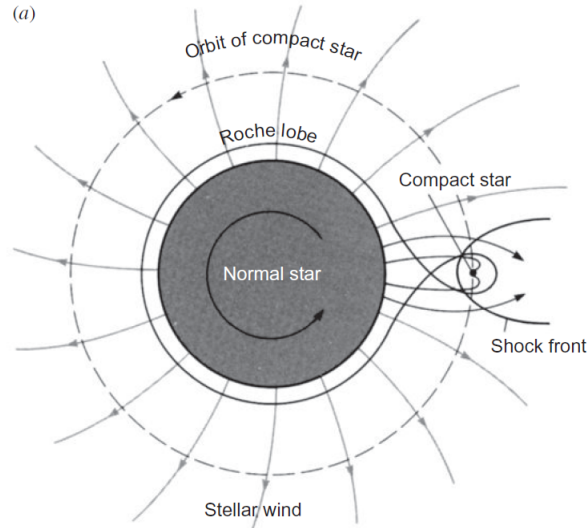


Figure 1.6: Illustration of a compact object deeply embedded in the stellar wind of a massive star (Longair 2011)

1.7 Vela X-1

Vela X-1 is the celestial object studied in this thesis work. It is a HMXRB system that consists of a NS emitting X-ray pulses and which orbits a B0.5 Ib supergiant companion star HD 77581 (Giménez-García et al. 2016). The system has an estimated distance of $2.42^{+0.19}_{-0.17}$ kpc, measured by the space observatory Gaia (Bailer-Jones et al. 2018), and is close enough that in spite of its moderate X-ray luminosity being $\sim 4 \times 10^{36} \text{ erg s}^{-1}$, it is one of the brightest X-ray sources in the sky (Nagase et al. 1986). From our line of sight (LOS) an eclipse is observed as a result of the system having an inclination

angle of 80° (Kretschmar et al. 2021). Based on the ephemeris (Kreykenbohm et al. 2008), the mid eclipse is defined at orbital phase $\phi_{orb} = 0$. Since the orbital separation is relatively small, $\sim 53.4 R_\odot$, the NS is deeply embedded in the strong stellar wind of the companion star.

The mass of HD 77581 is $21.5 \pm 4 M_\odot$ (Giménez-García et al. 2016), with a sturdy mass loss rate on the order of $10^{-6} M_\odot \text{yr}^{-1}$ (Kretschmar et al. 2021). Over the years the terminal velocity ν_∞ of the stellar wind has been determined by different authors, with the most recent estimates pointing to terminal velocities of $700_{-100}^{+200} \text{km s}^{-1}$ and $\sim 600 \text{km s}^{-1}$ (Giménez-García et al. 2016; Sander et al. 2018). The donor stars radius is about $30 R_\odot$ (Quaintrell et al. 2003), where it takes the NS ~ 8.9 days to orbit the supergiant (Forman et al. 1973). Given its low eccentricity of 0.0898 ± 0.0012 , the orbit of the NS is almost circular (Bildsten et al. 1997). The X-ray source has been observed to have a fluctuating pulse period of $\sim 283 \text{s}$ (McClintock et al. 1976), where the variation in the spin period results from the transfer of angular momentum of stellar wind accreting onto the NS surface.

Due to irregular variation in absorption and intrinsic X-ray flux, bright flares and “off-states” have been observed, where the short-term variability is thought to result from clumpiness in the wind (Kreykenbohm et al. 2008; Fürst et al. 2010; Martínez-Núñez et al. 2014; Haberl & White 1990; Kreykenbohm et al. 2008; Odaka et al. 2013; Martínez-Núñez et al. 2014; Sidoli et al. 2015). As for the geometry of the accretion structure, previous studies have shown through observation and simulation that the structure is composed of an accretion wake, photoionisation wake and a possible tidal stream. (Blondin et al. 1990; Manousakis & Walter 2015; Kaper et al. 1994; van Loon et al. 2001; Malacaria et al. 2016).

1.8 Spectral Features

The accretion structure of Vela X-1 is complex and not known in detail despite the vast amount of research that has been done on the HMXB by numerous authors. The observed X-ray spectrum of Vela X-1 is our primary tool to understand the accretion structure in the system. In this section I will discuss the different spectral models relevant to this work.

The Tuebingen-Boulder Interstellar Medium Absorption Model

As X-ray radiation passes through an interstellar medium (ISM) absorption may take place. This model calculates the cross section for X-ray absorption by the ISM. The total photoionisation cross section of the ISM is the sum for three different components.

$$\sigma_{ISM} = \sigma_{gas} + \sigma_{molecules} + \sigma_{grains} \quad (1.6)$$

Where σ_{gas} is the gas-phase ISM, σ_{grains} is the grain-phase ISM and $\sigma_{molecules}$ is the molecules in the ISM.

The contribution to σ_{ISM} from grain shielding is extremely small. For the molecular component only the cross section of hydrogen is taken into consideration. As for the gas-phase the cross-section of different photoionised elements is calculated and weighted by the abundance of each element. When using the model the hydrogen column is left to vary, giving rise to the parameter N_H , which is the equivalent hydrogen column given in units of 10^{22} atoms cm^{-2} (Arnaud et al. 2021; Wilms & Allen 2000).

Optically-thin Compton Scattering Correction

Compton scattering regards a photon interaction with a charged particle, typically an electron. In this interaction the photon loses energy, which is then transferred to the electron. In the low energy limit of Compton scattering where the photon has energy less than the electron energy, and if the electron is non-relativistic, then there will be no exchange of energy between the photon and electron. This regime is known as the Thomson scattering regime (Santangelo 2021a). This model makes a correction from the Thomson cross-section to the Klein-Nishina cross-section at high energies. In this work a non-relativistic Compton scattering correction is applied. This is because the Thomson cross section is larger than the Klein-Nishina cross section at higher photon energies and stays constant, whereas the Klein-Nishina cross section decreases as photon energy increases. Therefore, the hydrogen column density will be overestimated if the Klein-Nishina correction is not applied to the Thomson cross section. The model allows N_H to vary, which is the hydrogen column given in units of 10^{22} atoms cm^{-2} (Arnaud et al. 2021). The model is shown in equation 1.7:

$$M(E) = \exp(N_H \sigma_T(E)) \quad (1.7)$$

Where N_H is the hydrogen column density and $\sigma_T(E)$ is the Thompson cross section, which is dependent on the energy E .

Power Law With High Energy Exponential Cut-off

The X-ray spectrum of Vela X-1 was found to be best modelled by a power law with a high energy exponential cut-off (Nagase et al. 1986; Kreykenbohm et al. 1999). The model is shown in equation 1.8

$$A(E) = K E^{-\alpha} \exp(-E/\beta) \quad (1.8)$$

Where parameter(par) 1 is α the power law photon index, par 2 is β the folding energy (E-fold) of the exponential cutoff given in keV and par 3 being the normalisation constant, K, given in photons/keV/cm²/s at 1 keV (Arnaud et al. 2021). A simple powerlaw model without a high energy cut-off is given by $A(E) = K E^{-\alpha}$ (Arnaud et al. 2021).

Spectral Lines

Spectral lines result from the emission or absorption of light in a quantum system. For example in an atom the energy levels for the electron are quantized, where the levels are described by principal quantum numbers, $n=1,2,\dots$, and the atomic number Z . This gives rise to the atomic structure where the energy levels are given by equation 1.9:

$$E_n = -\frac{\alpha^2}{2} m_e c^2 \frac{Z^2}{n^2} \quad (1.9)$$

In equation 1.9 α is the fine structure constant.

When a single photon interacts with the electron it can be absorbed, enabling the electron to transition from a lower energy level to a higher energy level. The electron can then spontaneously emit a photon and in the process will make the transition from the higher energy level to a lower energy level. In this case the excitation and de-excitation of the electron occurs as a bound-bound interaction.

Transitions that correspond to certain energy levels are categorised into different transition series. For example transitions to n_1 from higher energy levels are part of the Lyman series, where L_α is the transition from n_2 to n_1 , L_β is the transition from n_3 to n_1 , L_γ is the transition from n_4 to n_1 and so on. The same goes for the Balmer and Paschen series however the transitions correspond to n_2 and n_3 respectively. In the case where the electron is freed from the system the atom is ionised. This transition is a bound-free interaction and is shown in figure 1.7, along with the first three transition series (Santangelo & Grinberg 2021).

In the spectrum these lines are modelled with a Gaussian which is shown in equation 1.10:

$$A(E) = K \frac{1}{\sigma\sqrt{2\pi}} \exp\left(-\frac{(E - E_l)^2}{2\sigma^2}\right) \quad (1.10)$$

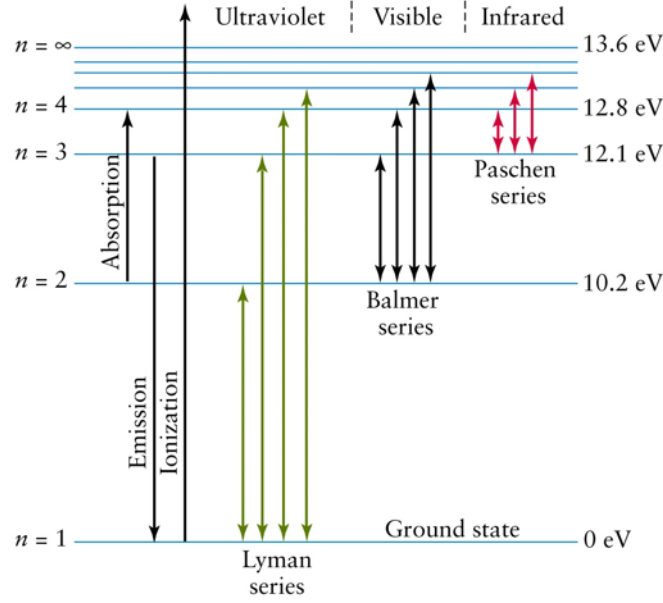


Figure 1.7: Schematic diagram of the different transition series (Santangelo & Grinberg 2021)

There are 3 parameters that come from this model. Par 1 is E_l , the line energy given in keV, par 2 is σ , the line width given in keV and par 3 the normalisation constant K given in total photons/cm²/s (Arnaud et al. 2021).

Spectral Triplets

If spin and relativistic corrections are also taken into consideration, then there will be spectral line splitting, which leads to the fine structure of the atom and a more complicated energy level distinction. For the electrons there are constraints on the possible transitions. Which transitions are allowed depends on the atom or ion.

It is important to note that in this work ions are categorised by the number of electrons bound to nuclei. For example if an atom heavier than hydrogen has lost all but one electron due to ionisation, it is a single electron system, which we treat as a Hydrogen-like atom. If an atom heavier than Helium has lost all but two electrons, then we treat it as a Helium-like atom and so on.

In order to make sense of the selection rules we must consider the electron spin which is denoted by \mathbf{S} , the orbital angular momentum denoted by \mathbf{L} and the total angular momentum, which is the sum of the electron spin and orbital angular momentum, $\mathbf{J} = \mathbf{L} + \mathbf{S}$. These properties have corresponding quantum numbers. For He-like ions the transitions must satisfy the following selection rules: $\Delta\mathbf{S} = 0$, $\Delta\mathbf{L} = \pm 1$,

$\Delta J = 0, \pm 1$ (Eisberg & Resnick 1985; ASTRO-H CookBook Members 2015). From the allowed transitions there are four strong emission lines, namely resonance (R), forbidden (F), and two intercombination (I) lines often treated as one line (x+y), which are shown in Figure 1.8. In the spectrum these lines are observed as triplets. The minimum number of electrons required for a triplet to occur is two (Yuichiro et al. 2021; ASTRO-H CookBook Members 2015). Each of the lines can be modelled with a Gaussian as outlined above in equation 1.10. Note that the energy level labelling terminology is used and is also described in Figure 1.8.

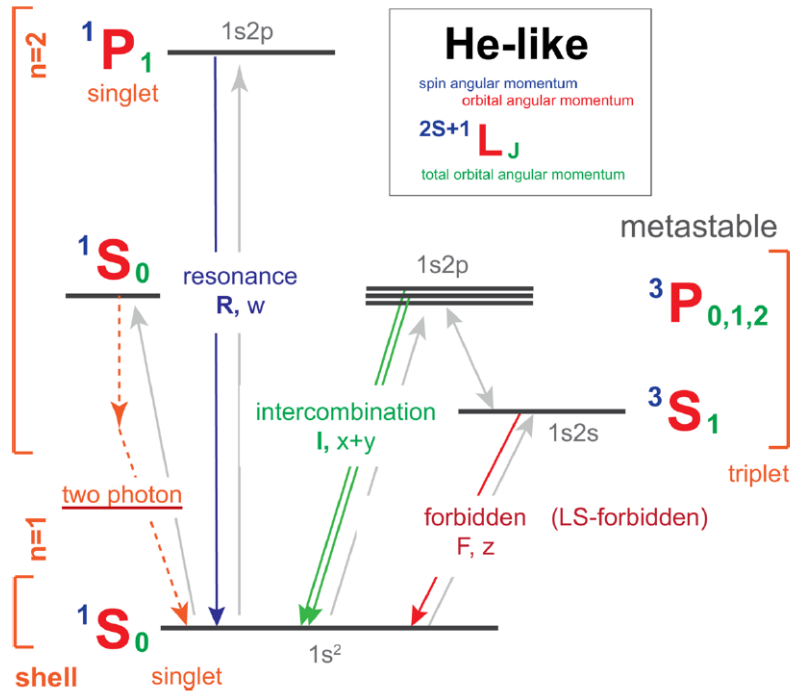


Figure 1.8: Schematic diagram of energy levels for He-like ions (ASTRO-H CookBook Members 2015)

Radiative Recombination Continua (RRC)

Radiative recombination occurs when an electron collides and recombines with an ion, emitting a photon in the process. In radiative recombination, the energy of the photon is equal to the kinetic energy of the electron plus the binding energy of the newly recombined electron. Since the kinetic energy of the electron is not quantized, this forms a continuous spectrum with sharp edges at the binding energy of the levels. The RRC model is given by equation 1.11

$$A(E) = \begin{cases} 0 & \text{if } E < E_e \\ K(1/T_p) \exp\left[\frac{-(E-E_e)}{T_p}\right] & \text{if } E \geq E_e \end{cases} \quad (1.11)$$

Where par 1 is E_e the energy threshold, par 2 is T_p the plasma temperature given in keV and par 3 is the normalisation constant K , given in photons/cm²/s (Arnaud et al. 2021).

1.9 Doppler Effect

The Doppler effect is the change in wavelength in relation to an observer who is moving relative to the wave source. For example if a star is moving away from an observer the wavelength of the radiation will stretch and appear red shifted, however, if it moves towards the observer then the wavelength will shorten and appear blue shifted. The Doppler effect can be used to calculate the velocity of the emitting wave source where the expression is given by (Santangelo 2021b):

$$v = \frac{\Delta\lambda}{\lambda_0} c \quad (1.12)$$

Here $\Delta\lambda$ is the changing wavelength for the moving source, λ_0 the wavelength for a stationary source and c the speed of light.

X-ray Multi Mirror Mission

2.1 XMM-Newton

The X-ray Multi Mirror Mission (XMM-Newton) is 1 of the 4 missions managed by the European Space Agency (ESA) as part of the Horizon 2000 Program. Aboard XMM-Newton are three Wolter type-1 X-ray telescopes and a 30-cm optical/UV telescope. For each telescope light is focused towards different detectors, which there are 3 types:

1. European Photon Imaging Camera (EPIC)
2. Reflection Grating Spectrometer (RGS)
3. Optical Monitor (OM)

In total there are six detectors, which can be operated independently or simultaneously. Figure 2.1 shows a sketch of XMM-Newton. Lower left shows two mirror modules that are equipped with reflection grating arrays. The focal X-ray instruments are positioned at the right end. The black/green horns are the EPIC MOS cameras. The EPIC pn camera is shown in violet and the RGS detectors in pink. The OM telescope is covered by the mirror module and so it can not be seen in this image.

Since the observation in this thesis did not make use of the 30 cm optical/UV telescope, and the OM detectors, they will not be discussed in detail (ESA: XMM-Newton SOC 2019).

2.2 Wolter Type-1 X-ray Telescope

Each of the Wolter type-1 telescopes on board XMM-Newton consist of 58 cylindrical grazing-incidence mirrors that have gold coating and are nested in a coaxial configuration to obtain the highest possible effective area. Each mirror has a common focal point, where the focal length of each telescope is 7.5 m. Figure 2.2 shows how one of the telescopes are assembled. The paraboloid and hyperboloid mirrors are positioned such that the incoming X-rays are focused towards the detector with a shallow grazing angle of $30'$. This low angle enables the mirrors to reflect efficiently at high energies, particularly the 7 keV region (ESA: XMM-Newton SOC 2019).

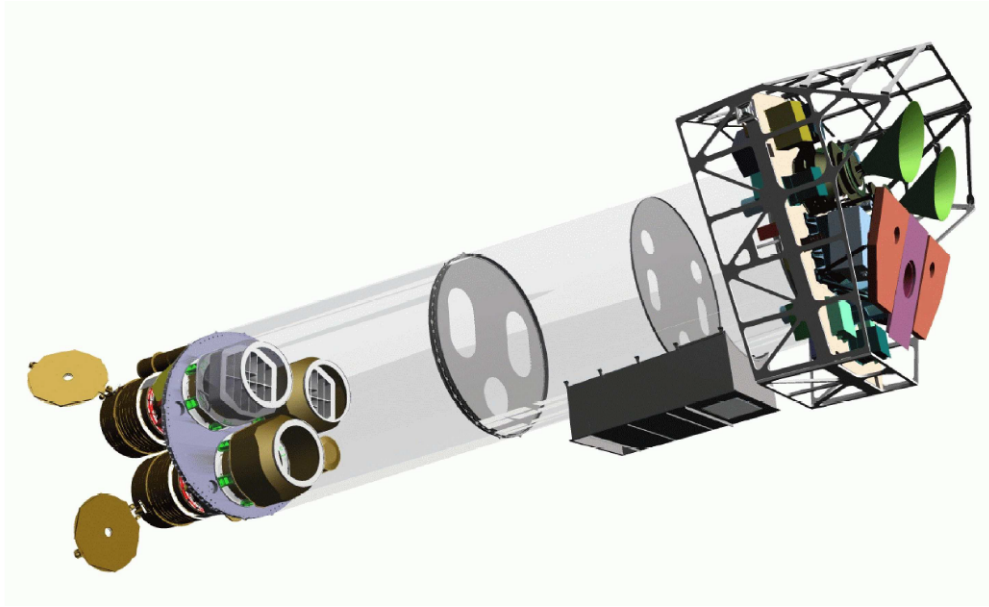


Figure 2.1: Sketch of the XMM-Newton (ESA: XMM-Newton SOC 2019)

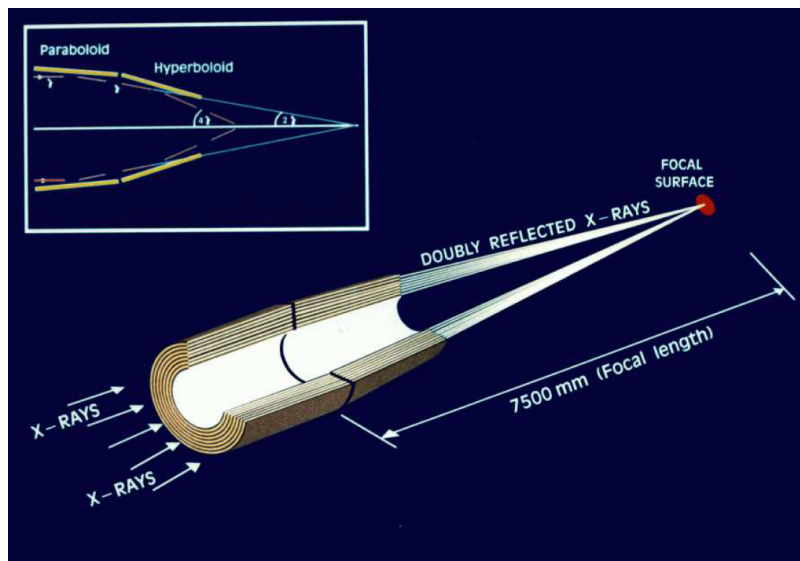


Figure 2.2: The light path and assembly of the Wolter type-1 X-ray telescope (ESA: XMM-Newton SOC 2019)

Figure 2.3 shows how the other two telescopes are assembled. In this set up 44% of the incoming light is directed by the grazing-incidence mirrors towards the prime focus. A grating array is positioned in the light path so that 40% of the X-rays are dispersed onto the secondary focus. The remaining light is absorbed by the support structures of the reflection grating arrays (ESA: XMM-Newton SOC 2019).

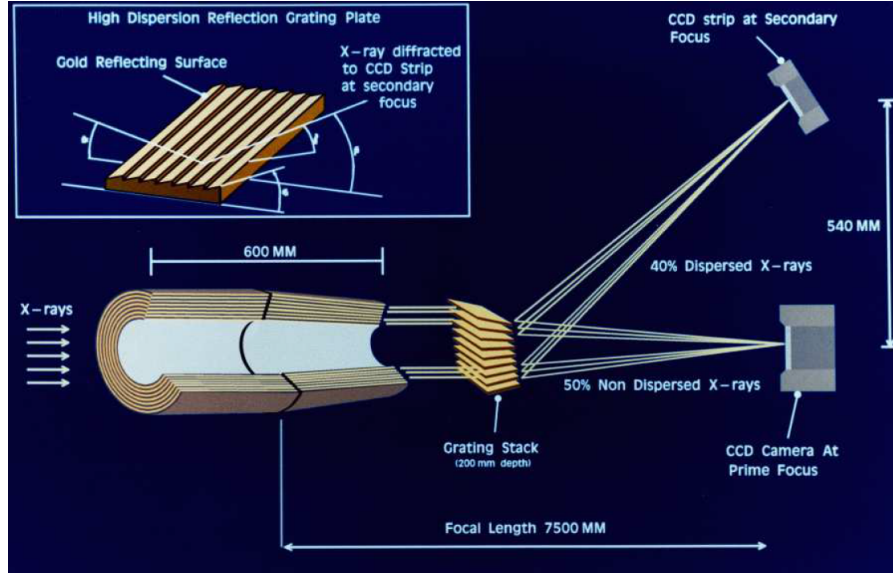


Figure 2.3: The light path of the other two X-ray telescope. Note the actual portion of light that is directed to the main focus is 44% (ESA: XMM-Newton SOC 2019)

2.3 Detectors

The two instruments that were used for the observation in this work are the EPIC and RGS detectors, which will be covered in detail in this section.

2.3.1 European Photon Imaging Camera

Two of the X-ray telescopes on board XMM-Newton are equipped with the EPIC Metal Oxide Semiconductor (MOS) Charged Coupled Device (CCD) arrays and the third telescope with the EPIC pn CCD camera. The EPIC cameras have a Field Of View (FOV) of $30'$ with an energy range from 0.2 to 12 keV. The spectral resolution is $E/\Delta E \sim 20 - 50$. The angular resolution has Full Width Half Maximum (FWHM) $\sim 6''$, which gives indication on whether two closely spaced spectral lines can be resolved. The Half Energy Width (HEW) $\sim 15''$, which indicates the detectability of a weak feature against a strong continuum. The pn time resolution for the timing mode and burst mode are 0.03ms and 0.007ms respectively. Figure 2.4 shows the field of view of the two EPIC cameras. On the left is the MOS camera and on the right the pn Camera. The shaded circles have a $30'$ diameter area (ESA: XMM-Newton SOC 2019).

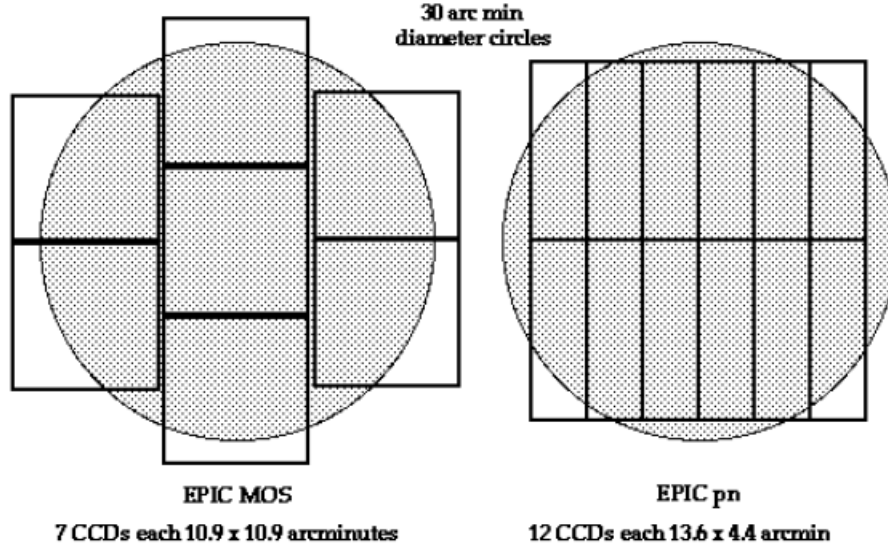


Figure 2.4: Layout comparison in the focal plane of the EPIC MOS and pn cameras (ESA: XMM-Newton SOC 2019)

2.3.2 Reflection Grating Spectrometers

Two of the X-ray telescopes mentioned in section 3.1 are equipped with RGS units, RGS 1 and RGS 2. These instruments are best suited for high resolution spectroscopy and have resolving power from 150 to 800 over an energy range of 0.33 - 2.5 keV. Each RGS unit consists of a reflection grating array which diffracts a portion of the X-ray light and is then focused by the mirror module to the RGS detectors as shown in figure 2.3. The grating plates have an average groove density of about $645.6 \text{ lines mm}^{-1}$. The dispersion angle, is equal to approximately 8.3 and $12.7 \text{ mm } \text{\AA}^{-1}$ at 15 \AA for the first and second order, respectively. The back of the RGS MOS chips are illuminated, which helps to maximise the soft energy response. The exposed side has an aluminium coating which is used to suppress optical and UV light. Each chip has $1024 \times 768 (27\mu)^2$ pixels, where half of them, 1024×384 , are exposed to radiation and the other half are sheltered and used as a storage area before readout, which is shown in the bottom panel of figure 2.5. The top panel shows the CCD bench with 9 MOS CCD chips mounted to it with a slight curvature arrangement. Its important to note that for RGS 2, during the first week of operation, an electronic component in the clock driver of CCD 4 failed, which corresponds to an energy band of 0.5 - 0.6 keV in the spectrum. Early September 2000 the same happened with CCD 7 of RGS 1, which corresponds to 0.9 - 1.2 keV (ESA: XMM-Newton SOC 2019).

Some of the key parameters and characteristics of the instruments on board XMM-Newton are shown in table 2.1

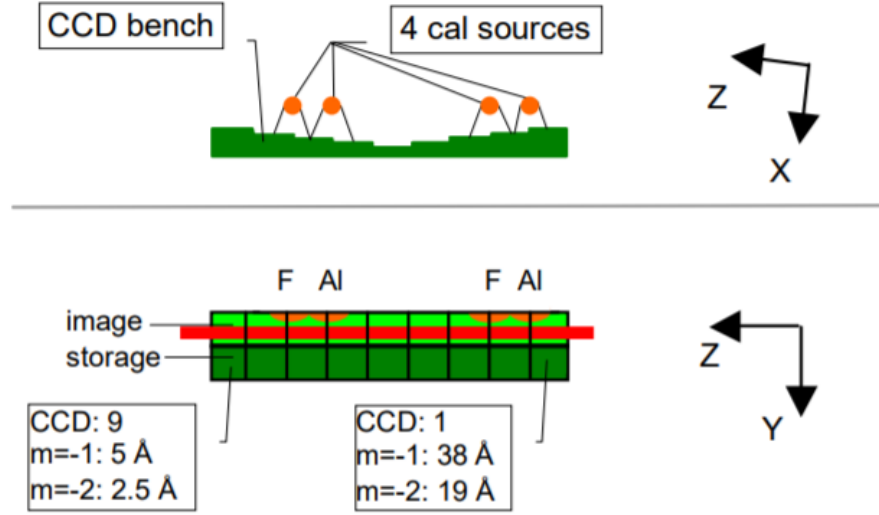


Figure 2.5: RGS MOS CCD bench arrangement (den Herder et al. 2000)

Table 2.1: Overview of XMM-Newton instruments (ESA: XMM-Newton SOC 2019)

Instrument	EPIC MOS	EPIC pn	RGS
Bandpass	0.15 - 12 keV	0.15 - 12 keV	0.35 - 2.5 keV
FOV	30'	30'	~5'
FWHM/HEW	5"/14"	6"/15"	N/A
Pixel size	14 μm (1.1")	150 μm (4.1")	81 μm (9×10^{-3} Å)
Timing resolution	1.75 ms	0.03 ms	0.6 s
Spectral resolution	~70 eV	~80 eV	0.04/0.025 Å

Data Reduction & Processing

An observation of Vela X-1 was made on November 2, 2000 lasting 59114s over an orbital phase from $\phi = 0.63$ to $\phi = 0.75$ using EPIC and RGS detectors on board XMM-Newton. The observation identification number (ObsID) is 0111030101 and is available from the NASA High Energy Astrophysics Science Archive Research Center (HEASARC), which is where the raw Observational Data Files (ODF) and calibration files for this work were retrieved. Both the data reduction and data extraction were conducted using the Science Analysis System(SAS) version 1.3 for both detectors.

3.1 EPIC

Instructions from the XMM-Newton ABC Guide, available from HEASARC, were followed in order to carry out the data reduction and data extraction process for the EPIC detector. Since the observation was made in the year 2000 it was necessary to rerun and generate the event files with the most recent calibration files, which was October 2020. With the SAS software, calibrated event files were generated using the task `epchain`. Standard filters, which included good event patterns, the preferred pulse height of an event and a canned screening were applied to the data using the `evselct` task. The next step was to extract the source and background spectra. The energy range specified, for the source event list was 500 to 1500 eV, again using the `evselct` task. Following this step a check for pile-up was executed.

3.1.1 Pile-up

Background

Pile-up is when multiple photons cumulate and cause an event in a Charged Coupled Device detector, which give a false reading. The two types of pile-up are classic pile-up and pattern pile-up. Classic pile-up is when multiple photons hit a single pixel. In this case the energy of each photon is summed, which can result in a high-energy component in the spectrum and a count rate that will be under estimated. Pattern pile-up is when neighboring pixels are hit by multiple photons. If the pixels that are

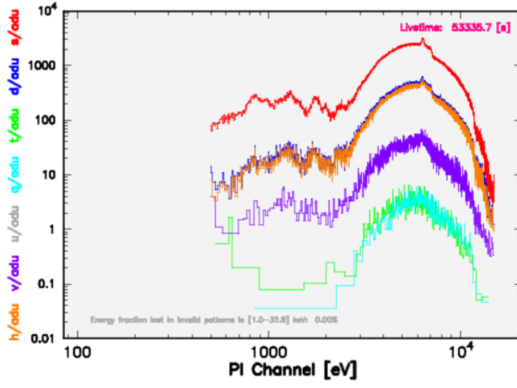
hit form a valid read out pattern then the photon energies will be incorrectly summed over (ESA: XMM-Newton SOC 2019).

Pile-up Correction

In order to correct for pile-up, an iterative approach was taken, where the removal of a chosen number of pixel columns either side of the boresight was implemented. This is analogous to imaging data, when removing regions with very high count rates. The process was repeated, with a different amount of columns removed for each iteration, until the model and observed pattern distributions agreed. In this work, 3 iterations were performed, where for the first iteration 1 column was removed, second, 2 columns removed, and the third, 3 columns removed. All further iterations, showed large error bars and too few counts. Figure 3.1, shows in the left panel the distribution of counts as a function of PI channel and in the right panel the expected pattern distribution plotted with observed distribution for different pattern classes. The top panel shows the data with no correction, the middle Panel 1 pixel column removed and the bottom panel 3 pixel columns removed. The iteration with 2 pixel columns removed is provided in the the Appendix, see figure 1.

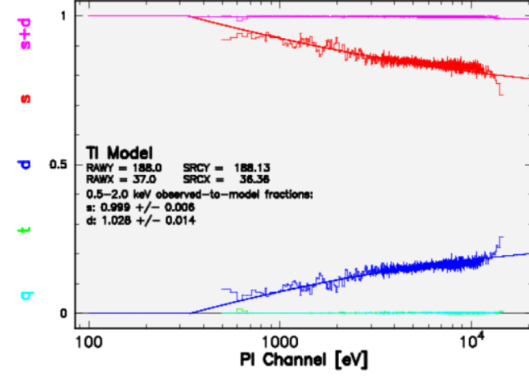
When checking for pile-up, the observed single and double event pattern distributions are the main factors when determining if an observation is affected by pile-up. Single patterns are shown in red and doubles in blue. As seen in the top-right plot, the observed pattern distribution deviates from the expected model, particularly at higher energies around 10^4 eV, indicative of pile-up in the data. Therefore, a pile-up correction was necessary. When 1 pixel column was removed, analysing the middle-right plot, there is an improvement between the model and observed pattern distributions at higher energies. However at lower energies the observed pattern distribution starts to deviate a little more. Fortunately, this is not too much concern because RGS data will be the primary instrument to analyse lower energies. Although the bottom panel shows better agreement between the model and observed pattern distributions, in the bottom-left plot, the number of counts observed are really low. Also the error bars are quite large compared to the left plots of previous iterations. Therefore it was decided that removing 1 pixel column either side of the boresight was the best extraction to go with in order to do deal with pile-up. Now that pile-up had been corrected for, the next step was to find the source and background region areas using the task `backscale`. This takes into account any bad pixels or chip gaps, and writes the result into the BACKSCAL keyword of the spectrum table.

XMM / EPIC pn FastTiming Thick



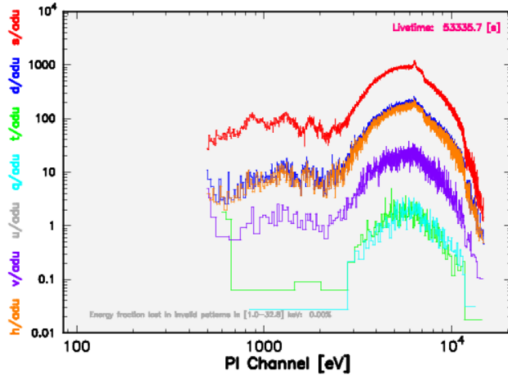
(a) No correction

PI Channel [eV]



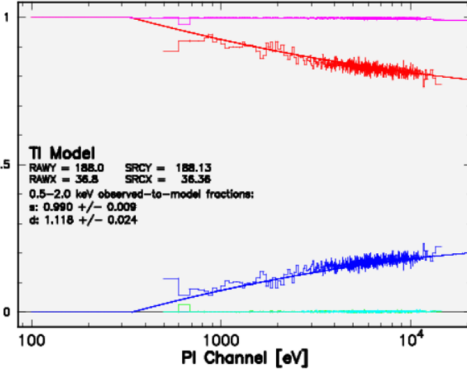
(b) No correction

XMM / EPIC pn FastTiming Thick



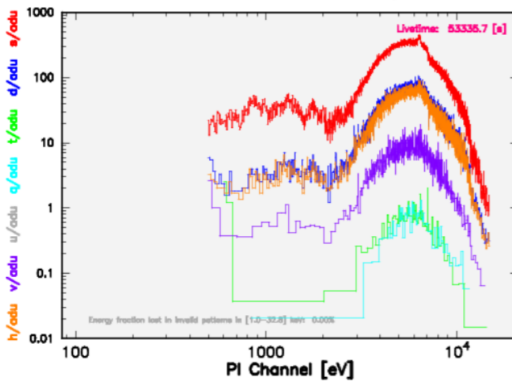
(c) First iteration

PI Channel [eV]



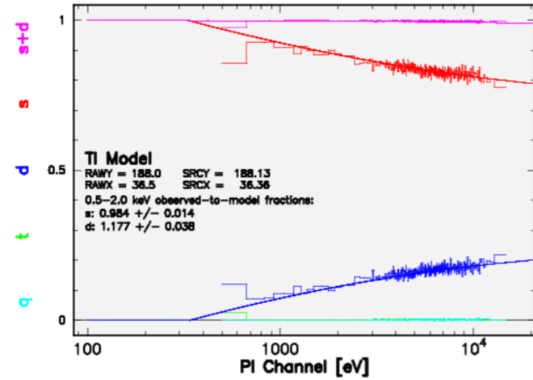
(d) First iteration

XMM / EPIC pn FastTiming Thick



(e) Third iteration

PI Channel [eV]



(f) Third iteration

Figure 3.1: Left: Distribution of Counts vs PI channel for each pattern Class. Right: Expected pattern distribution plotted with Observed distribution. The top to bottom panel show the first, second and third iterations respectively

3.1.2 Response Files

During the process of data reduction, an important factor is generating response files to protect the user from the complexity of the instrument response which varies across the field of view.

Redistribution Matrix File (RMF)

The RMF is defined as:

$$R_i(h, \epsilon) = \frac{\int_{E_{\epsilon-1}}^{E_{\epsilon}} R(h, E) dE}{(E_{\epsilon} - E_{\epsilon-1})} \quad (3.1)$$

Where, $R(h, E)$ is the detector response, which is a continuous function, at discrete energies E_{ϵ} . The RMF is used to redistribute and associate to each instrument channel (h) the appropriate photon energy (ϵ), (George et al. 2007).

Ancillary Response File (ARF)

The response of the detector to the incoming photons also depends on its sensitivity. The sensitivity is dependent on the mirrors and their ability to collect radiation at different photon energies. This information is described by an array of values given in the ancillary response file. In general the ARF gives the effective area of the detector system and reflects the ability of the mirrors to collect radiation at different photon energies and the quantum efficiency of the detector (George et al. 2007).

Response function

The response function of the detector is the $\text{RMF} \times \text{ARF}$ and is proportional to the probability that an incoming photon of energy (ϵ) will be detected in the output detector PI channel (h). To calculate the counts in each PI channel, the response function must be taken into consideration, and is given by the following integral:

$$C(h) = \int_0^{\infty} \sum_i R_i(h, \epsilon) A_i(\epsilon) S_i(\epsilon) d\epsilon dT + B(h) \quad (3.2)$$

Where $R_i(h, \epsilon)$ is the RMF, $A_i(\epsilon)$ the ARF, $S_i(\epsilon)$ the spectrum and $B(h)$ the background, which may or may not be detector specific (Nowak 2020). The function is integrated with respect to energy (ϵ) and time (T). The response files for the EPIC PN data in TIMING mode were generated with the following tasks. The task `rmfgen` was used to make the RMF and the task `arfgen` was used to generate the ARF. Once this was complete the spectrum was ready to be analysed.

3.1.3 Light Curves

In order to investigate the overall flux and the relative flux in different energy bands, the extraction of different light curves was carried out using the `evselect` task. During the extraction, given the low counts, a time bin size of 283s was used, which corresponds to one pulse period of the NS.

To generate the overall light curve an energy range from 0.6keV to 10keV was specified. 5 light curves of different energy bands were also generated to investigate the overall evolution and calculate the hardness ratios. The bands used in this work were 0.6-1, 1-3, 3-6, 6-8 and 8-10 keV.

3.2 RGS

The extraction process for both the RGS instruments was carried out following the step-by-step instructions titled “HOW TO REDUCE RGS DATA AND EXTRACT SPECTRA OF POINT-LIKE SOURCES, available on the ESA website: <https://www.cosmos.esa.int/web/xmm-newton/sas-thread-rgs>. With the SAS environment already set up, the task `rgsproc` was implemented to generate the following files listed below:

- Filtered event list
- Source list
- First and second order source+background spectrum
- First and second order background spectrum
- First and second order response matrix
- First and second order combined fluxed spectrum
- First and second order source lightcurve
- First and second order background lightcurve

Once the files were created, the source list was opened using fits view (fv), which is an easy to use graphical program for viewing FITS format files, to navigate through and confirm that the proposal coordinates were the same as the established coordinates of Vela X-1 taken from the HEASARC website. Thus, no modification to the proposal coordinates was needed.

The next step was to create spatial/order images using the `evselect` task. In order to display the images, that is, Top: The Cross Dispersion Angle vs Wavelength

(spatial) and Bottom: PI channel vs Wavelength (Order), with selected region masks overlaid for both instruments, the `rgsimpplot` task was executed, which the images for each instrument are shown in figures 3.2 and 3.3.

There were two important reasons to generate these images. First, the Processing Pipeline Subsystem (pipeline) products (PPS) were not used, since this was an old observation that needed to be rerun with the most recent calibration files. Thus, it was important to ensure all the sources in the RGS FOV were correctly identified, the selection regions centred on the prime source were correctly defined and the region used for background extraction excluded other existing sources. Second, after investigating how the observational data looked, see figure 2 in the appendix, multiple groupings at zero were observed. Therefore the wavelengths at where the data was close to zero needed to be checked, to see if they corresponded to dead CCD rows that would be visible as dark lines in the images. No dead lines were found, other than the expected dark regions from the damaged CCDs explained in section 3.3.2, and therefore dead CCD rows could be excluded as the cause of the groupings at zero.

Further analysis of the images, included making a comparison between the RGS 1 and RGS 2 instruments. As seen in figures 3.2 and 3.3, RGS 1 shows a large amount of noise in comparison to RGS 2.

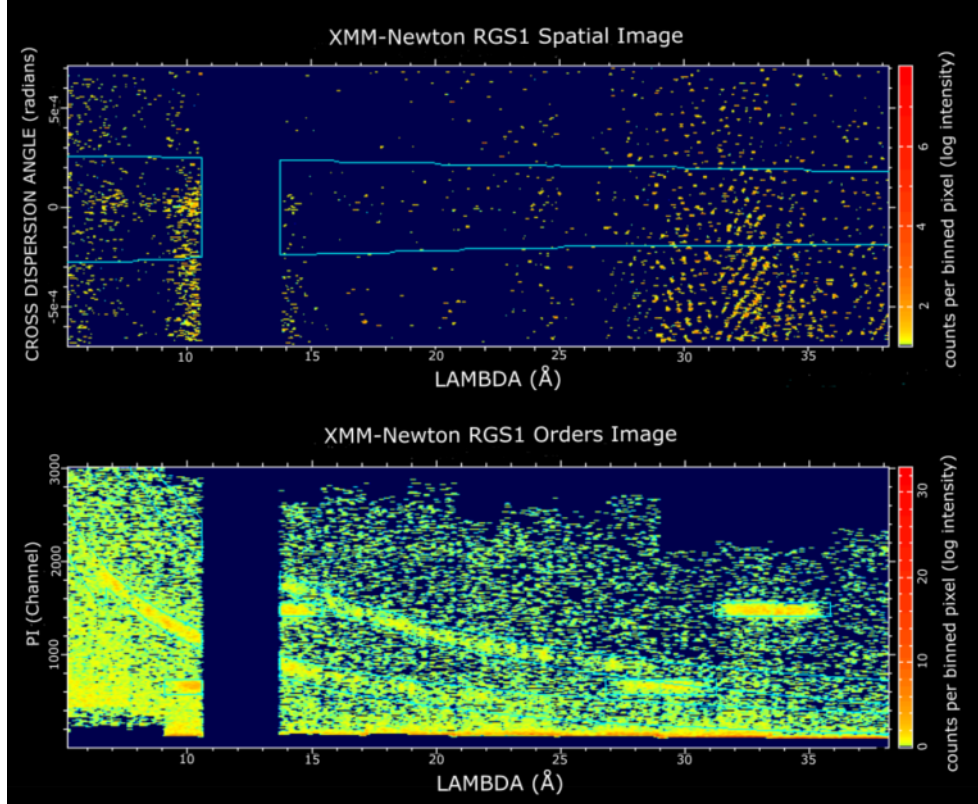


Figure 3.2: RGS 1 - Top: The Cross Dispersion Angle vs Wavelength. Bottom: PI channel vs Wavelength

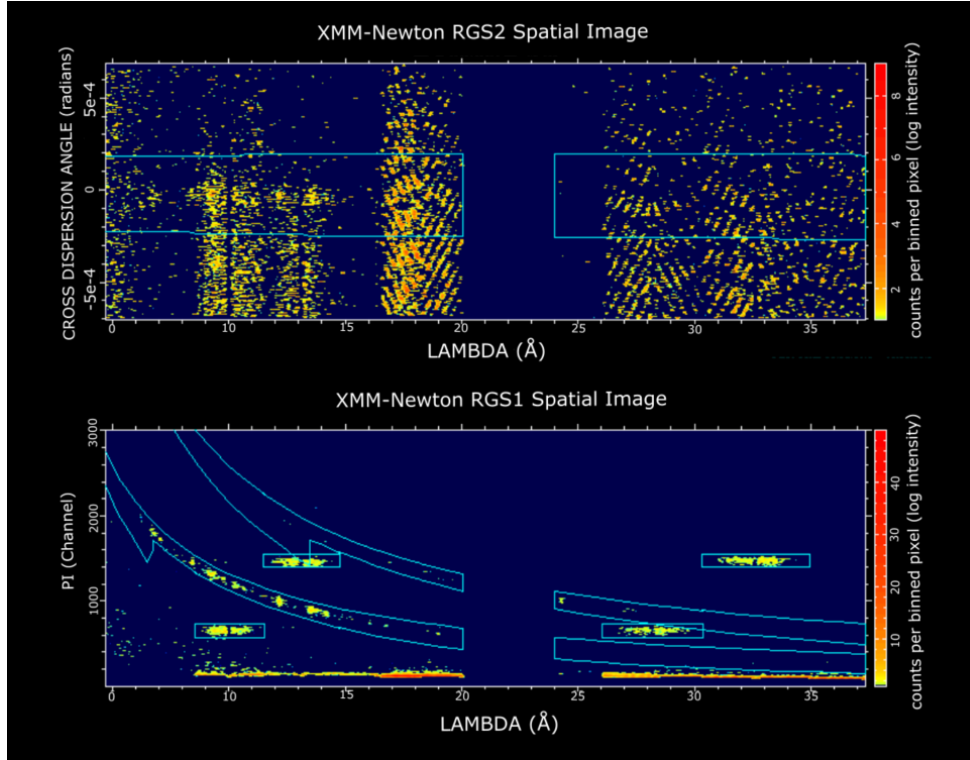


Figure 3.3: RGS 2 - Top: The Cross Dispersion Angle vs Wavelength. Bottom: PI channel vs Wavelength

3.2.1 Light Curve Extraction Issue

An attempt to create individual lightcurves for each RGS instrument using the `rgslccorr` task was carried out. During the extraction, the time bin size was set to 283s in order to have one pulse period per bin. The lightcurve for RGS 1 was generated successfully. However, when attempting to generate the lightcurve for RGS 2 an error was encountered. It stated that the ODF contains a different number of rows in the GTU and EXPOSU extensions, which should not happen. Included in the error was a recommendation to contact XMM-Newton Science Operations Center(SOC). After making contact with XMM-Newton SOC, they communicated that there was telemetry corruption in RGS 2 data, where no solution to fix all corrupted ODFs had been accomplished. It was therefore strongly recommended to do the analysis based on RGS 1 only.

Data Analysis & Results

Now that the data reduction and processing was complete, the goal was to create light curves and spectra for each detector using the Interactive Spectral Interpretation System (ISIS), a software package which can run scripts that are written in a programming language called S-lang. To produce the light curves and spectral models for each instrument, multiple coding scripts were written that made use of the ISIS functions (ISISscripts) provided by ECAP/Remeis observatory and MIT. The results and analysis are presented in this section.

4.1 EPIC

4.1.1 Light Curves

In order to investigate the overall variation in flux throughout the course of the observation, a light curve covering an energy range from 0.6 - 10 keV was extracted. Previous studies show that variations happen on all time scales from hundreds of seconds to thousands of seconds (Martínez-Núñez et al. 2014), however given the low counts for this observation, it made sense to extract the light curve with a time bin size of one pulse period, which is about 283 s. This is shown in figure 4.1, where the count rate (cts/s) is shown on the y-axis and the time (ks) is shown along the x-axis.

The time on the x-axis was initially given with reference to the Modified Julian Date (MJD), which is the number of days that have elapsed since midnight on November 17, 1858. In order to convert from MJD to seconds, the time of each event in the light curve time array was simply multiplied by $60 \times 60 \times 24$, the number of seconds in a day. Since the time values for each data point were initially given in MJD, an offset had to be determined and subtracted from each component. The offset is the time of the reference date (From which XMM-Newton data are recorded with reference to) to the observation start time (T-START). The MJD reference date (50814 MJD) and T-START (1037 days) were obtained from the fits view header file, where the offset was calculated by summing MJD reference and T-START and converting it to seconds giving 4.47989×10^9 s. Once the offset was subtracted from each time component, the array was then divided by 1000 in order to get units of ks.

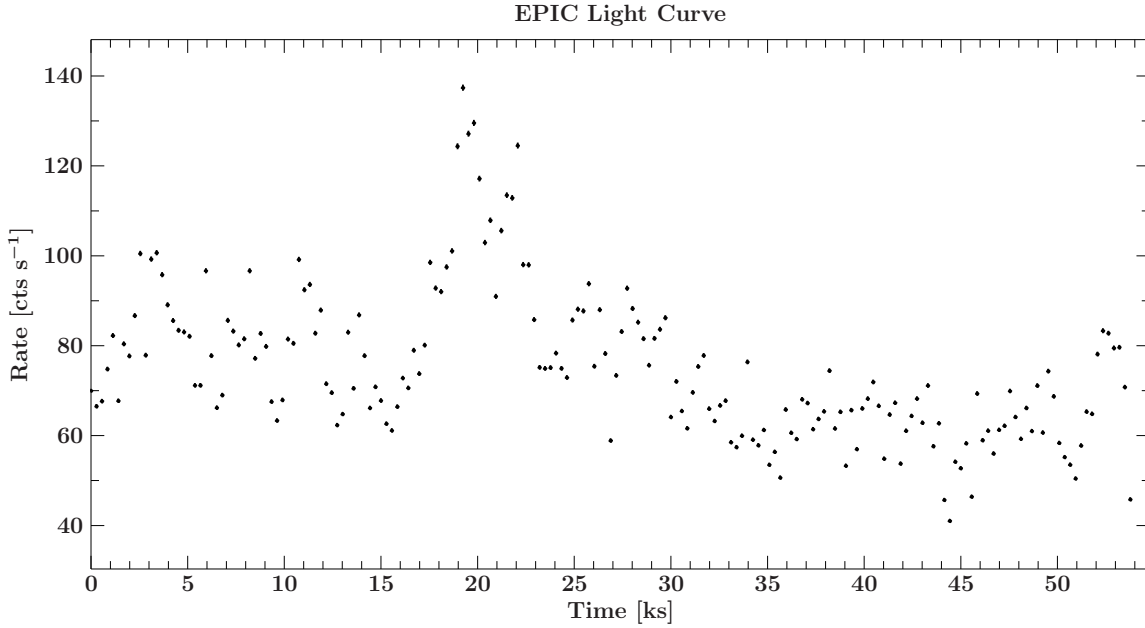


Figure 4.1: EPIC Light Curve. Note that the error bars are smaller than the data points

To describe the overall evolution of the observation and to explore the relative flux in different energy bands, multiple light curves were also extracted. The bands used were 0.6 - 1, 1 - 3, 3 - 6, 6 - 8 and 8 - 10 keV and were plotted together, see figure 4.2. The x and y axes are the same as for figure 4.1. A top axis is included, showing the orbital phase of the NS during the observation.

In order to calculate the orbital phase, a predefined function from the ISISscripts was used. It makes use of the equation $\phi = (T - T_0)/P_{orb}$, where T is the time given in MJD, T_0 is the MJD time corresponding to orbital phase 0, that is 52974.001 ± 0.012 MJD, and P_{orb} the orbital period, 8.96436 ± 0.00003 d (Kreykenbohm et al. 2008). Thus, both TSTART and TSTOP (which TSTOP is the end time of last frame) were inserted into the function to calculate the corresponding orbital phase and then used to scale the top axis.

Based on the light curve and its relative rates there is clear flux variation both overall and in each energy band throughout the entire observation, see figure 4.1 & 4.2. Given the small error bars, the intrinsic variation can be attributed to emission in the system rather than it resulting from background noise. During the first ≈ 16 ks of figure 4.2 there is relatively strong flux variation, which is most pronounced in the 6 - 8 keV energy band. Between ≈ 18 and ≈ 20 ks a large increase in brightness is observed, indicative of perhaps a weak flare, with contributions mostly from bands above 3 keV. From ≈ 20 ks to ≈ 23 ks the flare starts to decay. Following the flare, from ≈ 23 ks to ≈ 45 ks the source flux starts to decrease across all energy bands with

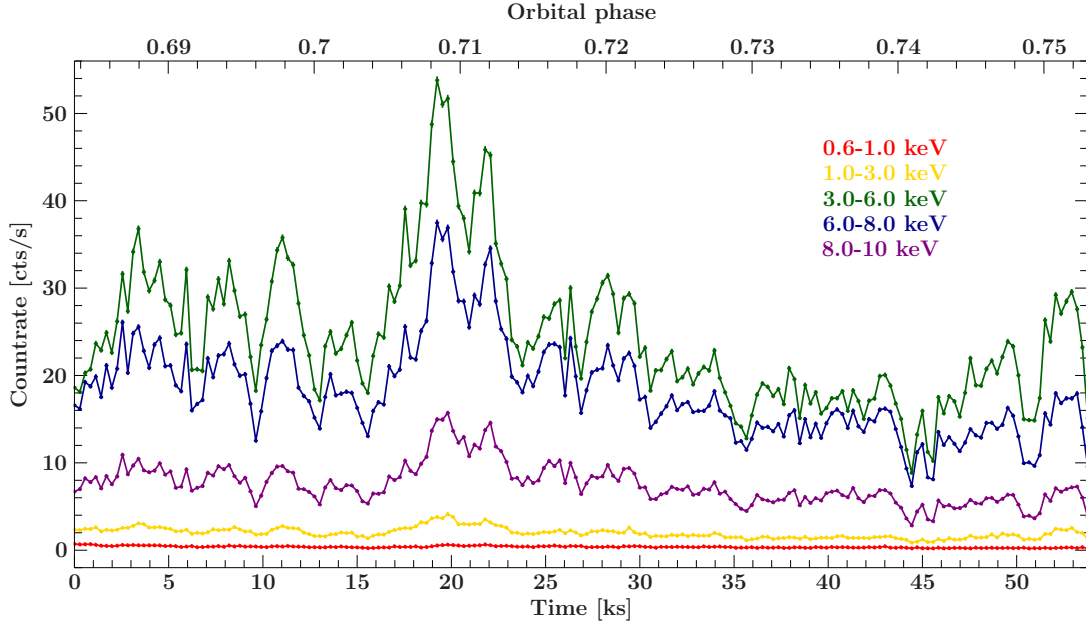


Figure 4.2: Light Curve of multiple bands. Note that the error bars are smaller than the data points

moderate variation. Beyond ≈ 45 ks to the end of the observation the source flux starts to rise steadily. Although the short term variability is mostly dominated by intrinsic flux variations, there is one standout feature observed, perhaps a weak flare, when considering the general evolution of the count rates across the entire observation. Such flares are thought to result from clumpiness in the stellar wind material (Martínez-Núñez et al. 2014). A plot displaying the light curves of multiple bands was also made with log scaled count rates, see figure 4.3.

This made the contribution from the least pronounced energy bands more visible. The plot also showed little change in variation in the 0.6 - 1 and 1.0 - 3 keV bands, however, displays a strong correlation across all energy bands.

4.1.2 Hardness Ratios

Hardness ratios give indication about the spectral shape and are used to gain insight about how the spectrum changes. The Hardness Ratio (HR) is given by the count rates in a Lower Energy Band (LEB) divided by the count rates in a Higher Energy Band (HEB):

$$HR = \frac{LEB}{HEB} \quad (4.1)$$

The 8 - 10 keV energy band in this data set is least affected by absorption because photons with higher energies have cross section that decreases as roughly $\hbar\omega^{-3}$ (San-

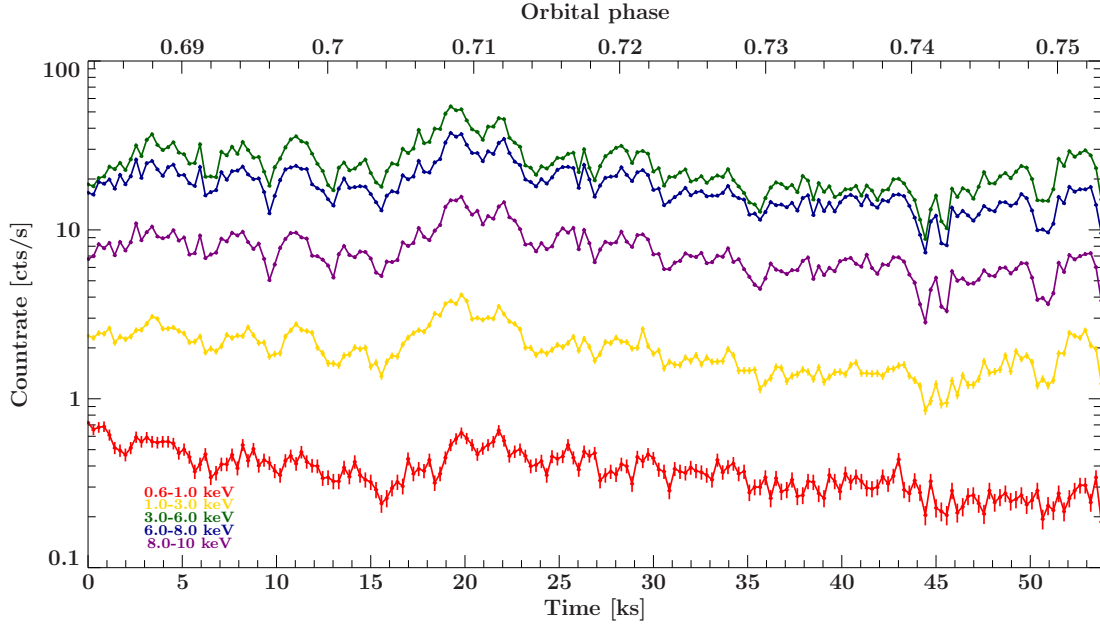


Figure 4.3: Light Curve of multiple bands with log scaled count rates. Note that the error bars are smaller than the data points

tangelo 2021a). Therefore the ratios were calculated with the first four bands divided by the 8 - 10 keV reference band. Plots for each flux ratio are shown in figure 4.4. From top to bottom they are displayed in the following order: 0.6 - 1 keV, 1 - 3 keV, 3 - 6 keV and 6 - 8 keV, where the left axis gives the hardness ratio, bottom axis the time in (ks), the right axis the total count rate and the top axis the orbital phase.

The light curves used to calculate the flux ratios were extracted with a time bin size of ~ 4 pulse periods, which is 1128 s. This was necessary, since the light curves in each energy band could be averaged over 4 data points, consequently making the hardness ratios less noisy and the general trend in each plot more obvious and clear. In the background of each plot the total flux evolution is included so a comparison with light curves can be made.

Figures 4.1 & 4.2 show the overall flux has strong variability, where the structures are highly correlated across all energy bands, see figure 4.3. The flux ratios are used to give indication of how the spectral shape changes for different evolutionary phases of the observation. In this work the largest variation in the flux ratios are mainly visible in the 3 - 6 keV and 6 - 8 keV energy bands. However, inspection of all energy bands, paying particular attention to the scale of the y-axis (they are different for each plot), you can see that there is no large change. The variation is stronger in the 3 - 6 keV and 6 - 8 keV bands, therefore it is no surprise that the global flux is mainly driven by higher contributions from higher energy bands. Even though there is some change observed in the flux ratios, this is not significant enough to effect the spectral shape

change at different phases of the observation. Therefore the data did not need to be divided into different spectra with smaller time exposures and could be executed for the entire observation.

4.1.3 Previous Modelling Efforts

The analysis related to the EPIC-pn detector in this work is built upon previous studies made by Martínez-Núñez et al. (2014). The knowledge and key findings obtained, which describe the evolution of the continuum for their observation, drives the interpretation and analysis in this work.

Martínez-Núñez et al. (2014) divided thier observation into 88 Epic-pn spectra each with 1.1 ks exposure. A phenomenological model enabled them to fit all 88 spectra throughout the entire observation, during which a flare had occurred. The continuum model consisted of three absorbed power law components, each with the same photon index and complemented by three fluorescent emission lines, **Fe K_α**, **Fe K_β** and **Ni K_α**. The model is shown below in equation 4.2:

$$\begin{aligned}
 F(E) = & \sum_{i=1}^2 [tbnew_i \times cabs_i \times Norm_i \times E^{-\Gamma}] \\
 & + tbnew_3 \times Norm_3 \times E^{-\Gamma} \\
 & + \sum_{j=1}^3 [tbnew_1 \times cabs_1 \times Gaussian_j]
 \end{aligned} \tag{4.2}$$

Where the summation index i corresponds to the three model components, and the index j corresponds to the three emission line components. $Norm_i$ represents the normalisation constant, and Γ the photon index for each power law component. Lastly, there is $tbnew_i$, an updated version of the Tübingen-Boulder ISM absorption model (Wilms & Allen 2000), and $cabs_i$, which is described in section 2.6.

Figure 4.5 is the modelled spectral fit for spectrum 15 of the 88 spectra in Martínez-Núñez et al. (2014), which was selected because it has the most resemblance to the observational data in this work. It is important to note however that all spectra had similar behaviour. The top panel shows the spectrum and the bottom panel, the residuals, which indicate how far the model is from the data. Components 1, 2 and 3 are shown in blue, green and red respectively, whilst the grey features are the emission line components. The observational data are plotted in black, where the y axis is the counts s⁻¹ cm⁻² keV⁻¹ and the x axis the energy given in keV

During their analysis they were able to trace the evolution of the continuum and absorption during the flare, which they proposed originated from a dense wind clump

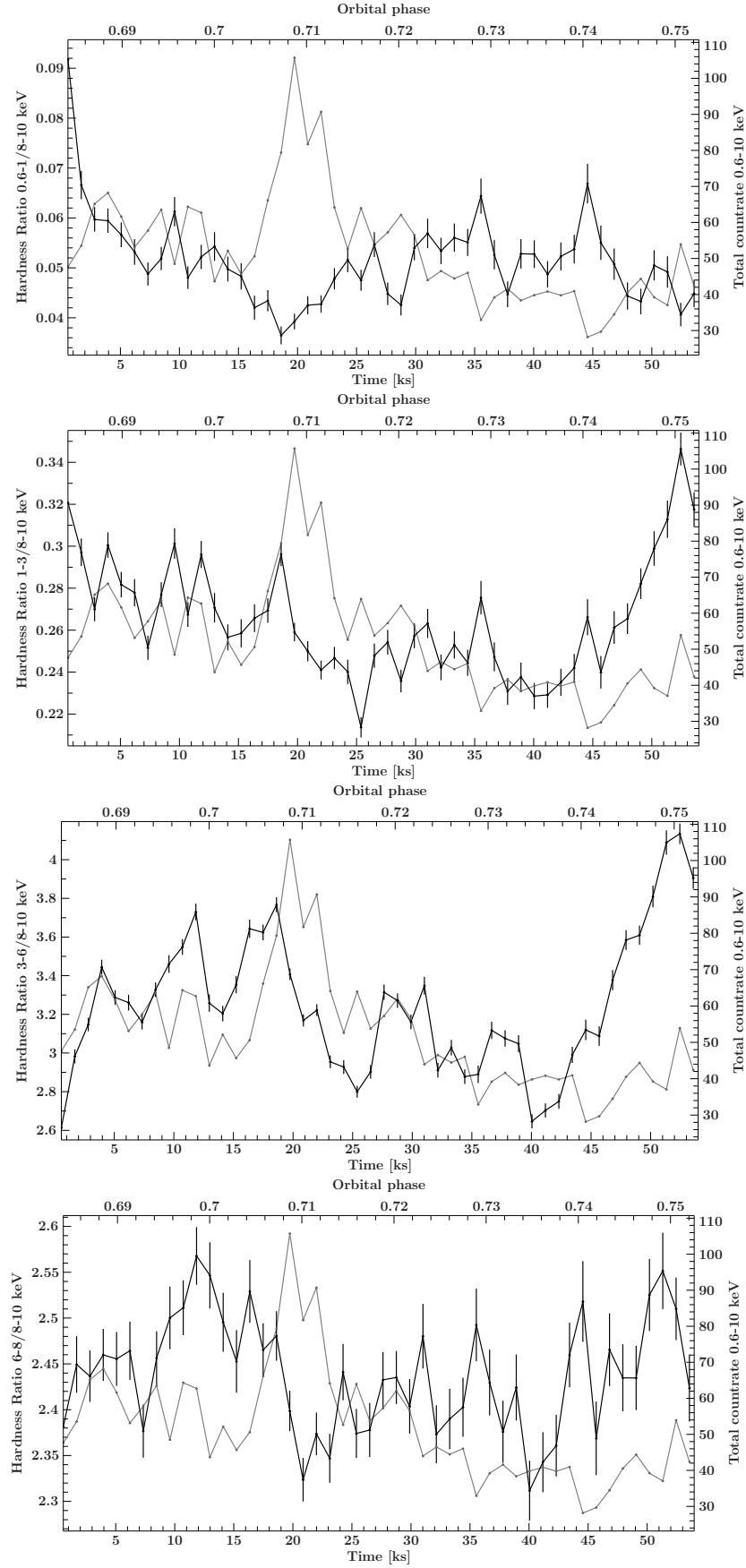


Figure 4.4: Hardness Ratios. *Top to bottom:* 0.6-1 keV, 1-3 keV, 3-6 keV and 6-8 keV

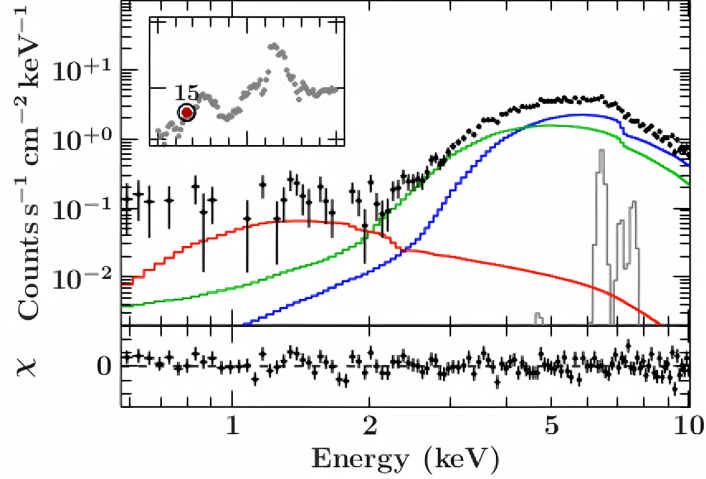


Figure 4.5: Spectrum 15 from Martínez-Núñez et al. (2014)

accreting onto the NS surface. Due to the ionisation state of the companion stars expanding envelope, absorption along our line of sight is extremely complex. However, they found that this could be successfully modelled by summing two cold absorption laws. The third component is thought to result from scattered emission by electrons in the wind. However, as seen in figure 4.5, the third component appears questionable or incomplete with possible emission lines that may need to be included. Given the uncertainty of the third component, a thorough investigation of the soft region was prompted in order to determine the contribution from emission lines and/or if the third component was necessary.

4.2 Chi-Square

The chi-squared (χ^2) test is a statistical hypothesis to see how well sample data fit a distribution of observed data points with a normal distribution. The goodness-of-fit shows the discrepancy between the observed values and those that would be expected from the model. The definition for χ^2 is given by equation 4.7:

$$\chi^2 \equiv \frac{(x_1 - \mu_1)^2}{\sigma_1^2} + \frac{(x_2 - \mu_2)^2}{\sigma_2^2} + \dots + \frac{(x_\nu - \mu_\nu)^2}{\sigma_\nu^2} = \sum_{i=1}^{\nu} \frac{(x_i - \mu_i)^2}{\sigma_i^2} \quad (4.3)$$

Where x_i are the independent variables, μ_i is the mean, σ_i^2 the variance and ν the degrees of freedom. This shows that χ^2 depends on the difference between actual and observed values, the degrees of freedom, and the sample size. Given that the values of x_i randomly fluctuate about μ_i , each term in the sum will be of order unity. Therefore if μ_i and σ_i are chosen correctly, we can expect the calculated χ^2 value to

be approximately equal to ν , indicating the model is a good fit to the data. If the calculated value for χ^2 is much larger than ν , then we can conclude that the data is not well described by the model (Press et al. 1992). Chi square test is used as the minimisation method to fit the spectrum for the EPIC-pn data.

4.2.1 Hard Spectrum

Given that there is no self-consistent physical model that can correctly describe the spectra of accreting X-ray pulsars, an empirical model was developed in this work. However, the development was guided by the model established in Martínez-Núñez et al. (2014). At the start of the fitting process, the first step taken, was to inspect how the spectral data behaved by plotting the data alone. In doing so, the hard region between 2.6-10 keV was chosen as the best place to begin the fitting process and investigate the parameters of each contributing component of the model. This was because the EPIC-pn detector does not have sufficient resolution to investigate the complexity of the soft region thoroughly, see figure 4.6. Additionally, the parameters for the hard region were constrained particularly well in previous work by Martínez-Núñez et al. (2014) to use as a guideline for the spectral fitting process.

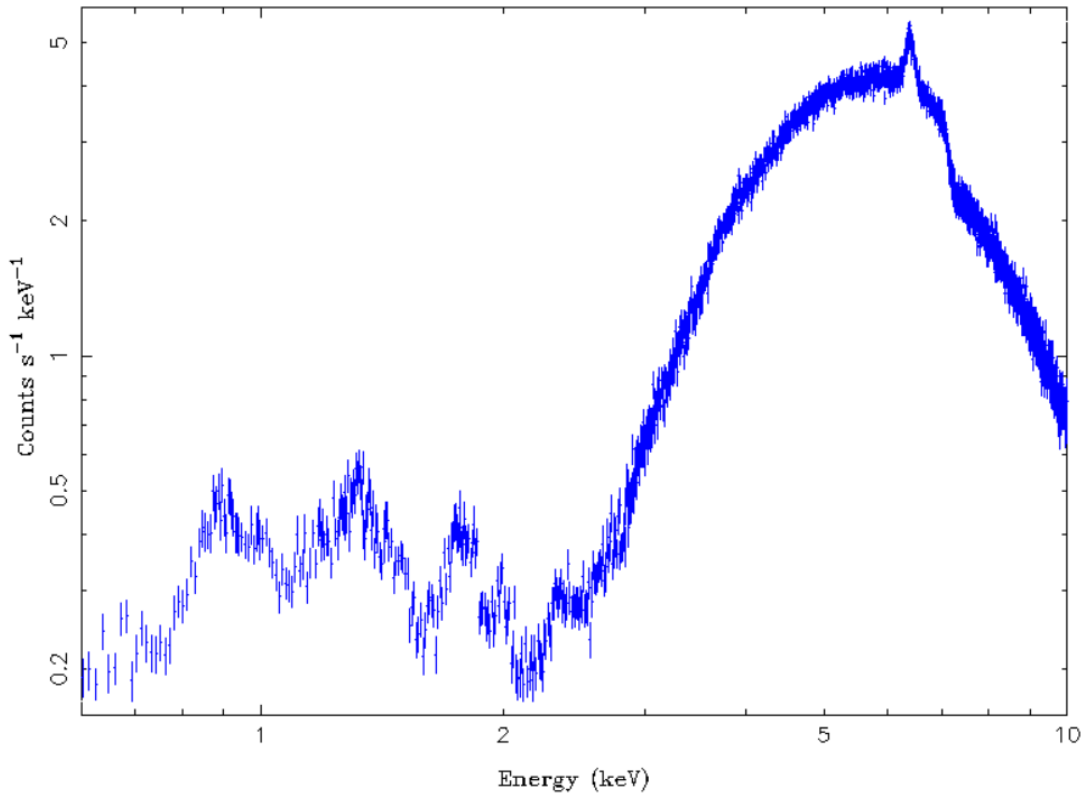


Figure 4.6: Spectral data (2.6-10 keV)

To get started, the energy range was re-scaled, so that the spectrum only showed data between the specified energy range for the hard region. Given the fairly low counts detected in each spectral bin, the data was re-binned in order to improve on the χ^2 statistics as a good minimisation method during the fitting process. As a general rule, the number of counts in each spectral bin should be greater than 20. The re-binning in ISIS is achieved by using the `group` function from the ISISscripts, which re-bins the spectra to a minimum signal-to noise ratio (SNR) and/or a minimum number of channels in each grouped bin. After exploring different values for the SNR, the optimal value found was 10, corresponding to an increased minimum value of about 100 counts per bin, whilst retaining a good resolution.

Absorption along the line of sight through the wind is complex due to the ionisation state of the companion stars expanding envelope. Martínez-Núñez et al. (2014) were able to model the absorption successfully by summing two conventional cold absorption laws. This was used as a basis for this work, however different models were also explored. After trying different models the model following Martínez-Núñez et al. (2014) was the best fit for the hard spectrum. It consisted of two absorbed power law components and two emission lines corresponding to the **Fe K $_{\alpha}$** and **Fe K $_{\beta}$** fluorescence lines. These were treated as being absorbed and modelled by a Gaussian function. The best fit model is shown in equation 4.4:

$$F(E) = \sum_{i=1}^2 [tbabs_i \times cabs_i \times Norm_i \times E^{-\Gamma}] + \sum_{j=1}^2 [tbabs_2 \times cabs_2 \times Gaussian_j] \quad (4.4)$$

Where, as explained for equation 4.2, the summation index i corresponds to the two model components, and the index j corresponds to the two emission line components.

The different components in the model, which are explained in section 2.6, were further modified due to two effects that both result from material, with column density N_H , covering the X-ray source. The first effect being the photoelectric absorption, modelled with *tbabs*, the Tübingen-Boulder ISM absorption model, and the second being the non-relativistic Compton scattering effect modelled with *cabs*, both of which are also described in section 2.6.

In this work the fitting process was carried out by allowing the parameters to vary and minimising the statistics. Following this approach the best possible fit statistics and best constraints of the relevant parameters were obtained for the hard region. Figure 4.7 shows the hard spectrum with the best fit model. The data points are plotted in blue, whilst the model and model components are shown in red. The

top panel is the spectrum and bottom panel, the residuals. Along the y axis is the $\text{counts s}^{-1} \text{keV}^{-1}$ and the x axis the energy given in keV.

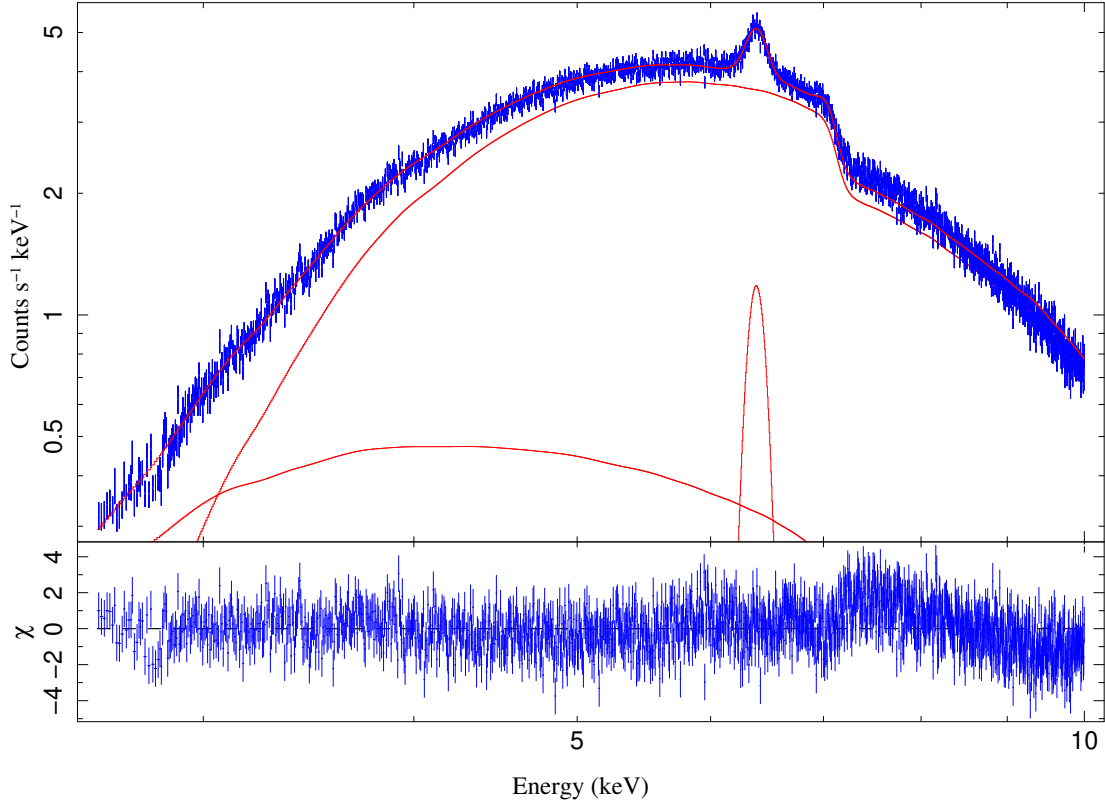


Figure 4.7: Hard Spectrum (2.6-10 keV)

As for the parameters, the photon index Γ for both power law components were tied together. The reason being is that the X-ray emission forming both power laws are thought to originate from the same place, near the NS surface. Therefore the slope of each power law component would be the same. The best fit value for the photon index was found to be $\Gamma = 1.606^{+0.02}_{-0.003}$. This value is very close to that determined by Martínez-Núñez et al. (2014), which the small inconsistency may be due to the response of the instrument. The absorption column density N_H for each power law component was left to vary, and thus had different values as a result of X-ray emission passing through different regions of the stellar wind material. Because both the absorption modification models are linked to a particular power law component, the N_H parameter for *cabs* and *tbabs* can be tied together. The best fit value for column density of component one was found to be $N_H = 13.46^{+2.26}_{-2.37} \times 10^{22} \text{ cm}^{-2}$, whilst for the second component was $N_H = 44.47^{+1.26}_{-1.12} \times 10^{22} \text{ cm}^{-2}$. To determine the fluorescence lines, the energy of the

Fe K_β line was constrained with respect to the center energy of the **Fe K_α** line. The best fit value for the center energy of **Fe K_α** was 6.387 ± 0.003 keV, which is very close to the theoretical value of 6.4 keV for neutral iron. Taking the theoretical calculation of 0.65 keV, by which the **Fe K_β** is shifted and then fixed, the center energy for **Fe K_β** was determined to be 7.037 ± 0.003 keV, which of course is also close to the theoretical value of 7.05 keV. This subtle inconsistency for both these measured values again could be due to the response of the detector.

Although the spectral fit had reduced $\chi^2 = 1.47$ (which if the reduced $\chi^2 \approx 1$ this indicates an excellent fit) between 7 keV and 8 keV, a bump in the residuals can be seen in figure 4.4. Here the model deviates from the data slightly. This corresponds to an energy range where the **Ni K_α** line is expected (Martínez-Núñez et al. 2014). An attempt to find this line was made with no success. It was then thought that the deviation might be caused by accidental shifts in the energy scale for specific pixels as a result of incorrect values in the offset map. A gain shift correction was then applied, an ISISscript function that applies a linear transformation to the energy grid of the model counts spectrum, which did improve the fit, however the parameter values, made no sense physically. To date, no solution or explanation for this bump in the residuals has been determined and therefore needs further investigation for the paper.

4.2.2 Total Spectrum

Now that the best possible fit to date, for the hard spectrum was complete, the next step was to extend the fit to the entire spectrum. In order to do this, the parameters found in section 5.1.4 were fixed. Whilst continuing to work with a SNR of 10, the energy range of the spectrum was then expanded so that it showed data between 0.6 - 10 keV. After trialing a few different models, the fit that best describes the data for the total spectrum is given in equation 4.5:

$$\begin{aligned}
 F(E) = & \sum_{i=1}^2 [tbabs_i \times cabs_i \times Norm_i \times E^{-\Gamma}] \\
 & + \sum_{j=1}^2 [tbabs_2 \times cabs_2 \times Gaussian_j] \\
 & + tbabs_3 \times [Norm_3 \times E^{-\Gamma} + \sum_{j=3}^5 Gaussian_j]
 \end{aligned} \tag{4.5}$$

As mentioned before, the modelled continuum proposed by Martínez-Núñez et al. (2014), see equation 4.2, forms the basis of this model. However, the difference lies in the three additional Gaussian functions that were incorporated. The purpose for this

was to investigate if and how much the emission lines in the soft region contribute to the third component.

Previous studies describe the origin of the third component as scattered emission in the wind. Meaning high energy X-ray photons emitted from near the neutron star surface interact with free electrons in the complex stellar wind material. During this interaction they are scattered into our line of sight and only experience a direction change. Collectively, these scattered photons are observed as an echo that form the third component at low energies, as it is low energy photons that are more likely to be scattered. Since the X-ray emission of all three components originate from the same place, the slope of all three components can be tied together. Thus the photon index for the third component also has value $\Gamma=1.606^{+0.02}_{-0.003}$.

Figure 4.8 shows the total spectrum with the best fit model from this work. An inspection of the plot reveals that the slope of the third power law component describes the soft region poorly and begs the question of its necessity. Given the three prominent features that resemble emission lines, to improve the fit, three Gaussian functions were added to the single absorption power law model, consisting only of *tbabs*. No *cabs* correction is needed here as this component describes an echo consisting of soft X-ray emission. An attempt to fit the emission lines to complement the third component was carried out to no real success, accredited mainly to the low resolution of the EPIC-pn detector. The features in the spectrum proved too difficult to pin down as emission lines, as they were too broad.

Based on the four different regions, outlined in table 4.1, where four different resonant transitions of highly ionised elements are expected (Lomaeva et al. 2020), the three prominent features visible in the spectrum sit in three of these specified regions. Previous studies on Vela X-1 show the existence of multiple narrow band features in these spectral regions, which suggests that these features could be made up of multiple emission lines and/or RRC (Lomaeva et al. 2020; Grinberg et al. 2017; Amato et al. 2021). From left to right, the first peak lies in the **Ne** region, second peak, the **Mg** region and the last peak in the **Si** region.

Table 4.1: Expected element regions

Main expected element	Energy range [eV]
O	300 - 900
Ne	800 - 1400
Mg	1200 - 1700
Si	1600 - 2100

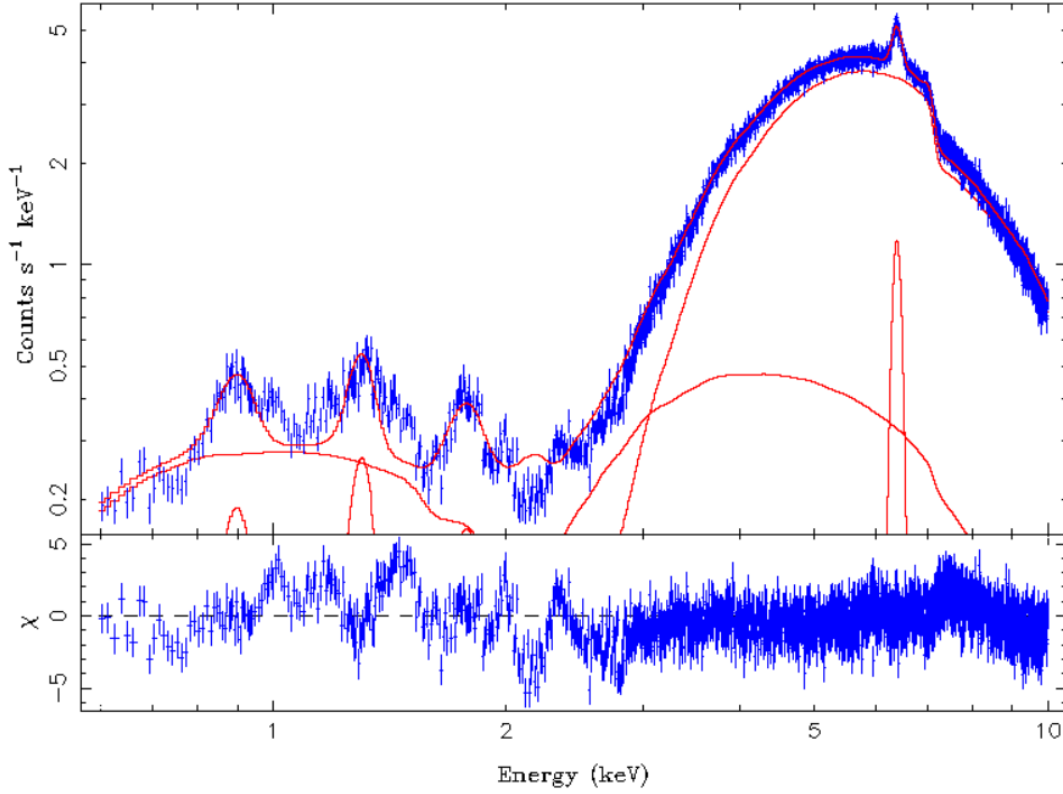


Figure 4.8: Total Spectrum (0.6 - 10 keV)

In order to do a thorough and proper investigation of the soft region, analysis utilising the RGS 1 detector and performing high resolution spectroscopy was required. The analysis with RGS 1 will be covered in the next section.

4.3 RGS 1

As mentioned in the introduction of this section, ISIS software was used to perform the spectral analysis. As a reminder, RGS 2 data was not available due to telemetry corruption, and therefore, the analysis was carried out using only the observational data of RGS 1.

4.3.1 Light Curve

The analysis in this section follows the work carried out by Lomaeva et al. (2020). They observed a strong flare during their observation, and conducted spectral analysis pre-flare, flare and post-flare. The light curves from the EPIC-pn detector for this work show the presence of a weak flare. Therefore to examine the overall flux and to investigate if the flare was detected by RGS 1, the light curve for the entire event list

was extracted with a time bin size of 283 s.

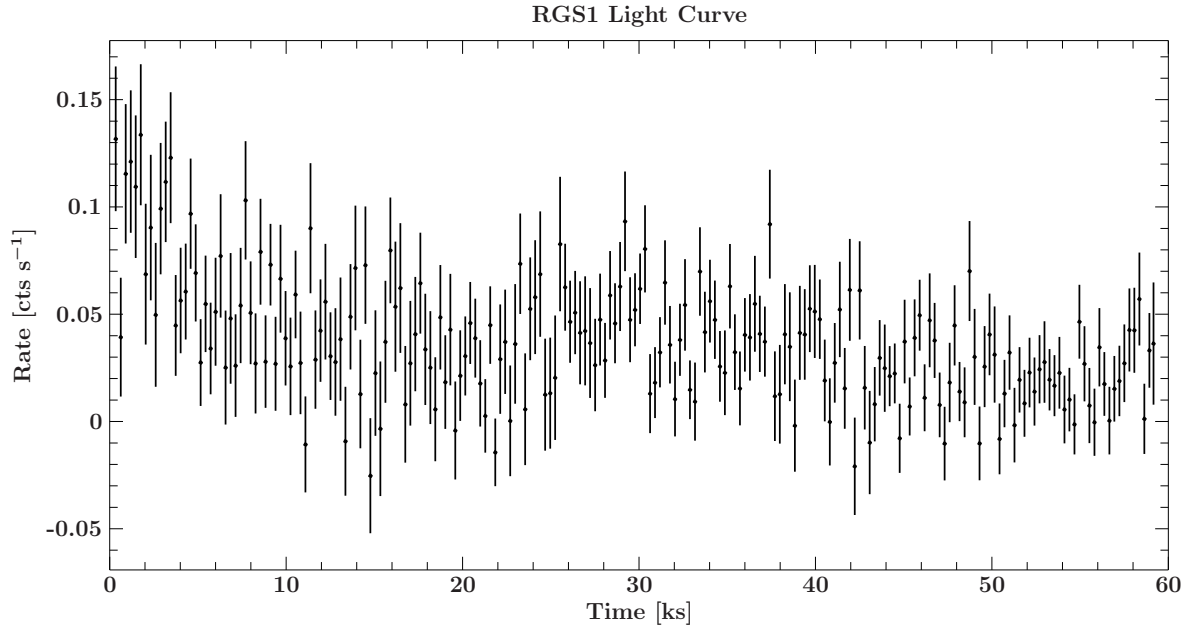


Figure 4.9: Light Curve of RGS 1

Across the light curve, no significant features or distinct behaviour is observed, see figure 4.9. The small flare present in figure 4.1 is not evident in the RGS 1 light curve. This is no surprise as comparing with figure 4.2, most contributions to the flare came from the energy bands above 3 keV. Moreover there are large error bars, meaning the data is strongly affected by background noise. As no significant features are seen in the data, there was no need to extract spectra for different phases and therefore the spectral analysis was performed for the entire observation.

4.4 Cash Statistics

Like χ^2 statistics, Cash statistics test how well sample data fit a distribution of observed data points, but the data points follow a Poisson distribution rather than a normal distribution, which is the case for χ^2 statistics. To assess the quality of the fit one must make use of the likelihood function, which is defined as:

$$L = \prod_i \frac{M(i)^{D(i)}}{D(i)!} \times \exp[-M(i)] \quad (4.6)$$

Where $M(i) = S(i) + B(i)$ is the sum of the source and background model amplitudes, and $D(i)$ is the number of observed counts in bin i . Using the likelihood function the cash statistics can be derived, see Cash (1979), which is defined as:

$$C = 2 \sum_i [M(i) - D(i) \log M(i)] \quad (4.7)$$

Where the factor of 2 exists such that ΔC is distributed as approximately $\Delta \chi^2$ when the number of counts in each bin is greater than 5. Therefore ΔC can be used instead of $\Delta \chi^2$ as a model comparison test, particularly for data with low counts (Cash 1979). Cash statistics are therefore used as a minimisation method for the RGS 1 instrument.

4.4.1 High-resolution spectroscopy

The main goal of this thesis is to determine the accretion structure of Vela X-1. This involves, verifying if there is an echo in the wind structure, and if so, investigating the contribution to the third power law component from emission lines and RRC. Therefore, high resolution spectroscopy is performed in order to address these matters. For the paper a further step involving plasma diagnostics will also be carried out and will be covered briefly in the discussion.

4.4.2 Continuum Model

As shown in section 5.1.5, modelling the soft X-ray emission was especially challenging. The development of the continuum model for RGS 1 data builds upon the empirical model in section 5.1.5, and in particular the third power law component. To begin the fitting process, the energy range for the spectrum was specified as 0.6 - 2.1 keV, followed by an inspection of the data within this energy band. Mainly to check how the data behaved and if any groupings at zero remained. No major groups were found, however, damage to CCD 7 created a blind spot between $\sim 0.9 - 1.2$ keV, see figure 2 in the appendix. Given the low counts observed in each spectral bin, an optimal re-binning for the data was implemented using the `rebin_dataset_optimal` function, which follows the guidelines outlined in Kaastra & Bleeker (2016). A "Simplex" algorithm for solving unconstrained optimisation problems was also set with the minimisation method based on Cash statistics.

4.4.3 Absorbed Power Law

During the analysis, comparisons were carried out for three different models with different parameters and model components to determine the best model that describes the overall continuum shape for the soft region of the spectrum.

The first model involved fixing the best fit parameters (the density column N_H , the photon index Γ and the normalisation constant K), obtained in section 5.1.5. This was followed by a second fit, where the parameters were left free to vary, and the best fit values obtained. Given the higher resolution of RGS 1, it was expected that the parameters would be improved upon.

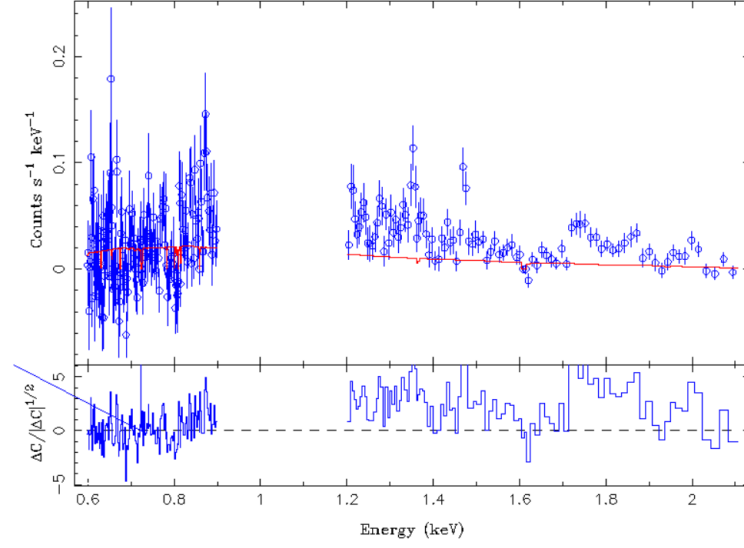
Figure 4.10 shows a comparison between both models, with the top figure (a), displaying the first spectral fit, and figure (b), showing the second spectral fit. For each figure the observational data is plotted in blue and the model in red. The top panel shows the spectrum with counts $s^{-1} \text{ keV}^{-1}$ along the y-axis and energy in units of keV along the x-axis. In the bottom panel the residuals are displayed.

The general shape of the model in figure (a) shows a lack of consistency with the data, which was expected given the results derived in section 5.1.5. The slope of the power law appears to have a fairly flat shape, in contrast to the data, which has an upwards trend between 0.6-0.9 keV, and downwards trend between 1.2-2.1 keV. The deviation between model and data, lead to a reduced cash statistical value of 5.81. In figure (b), the power law shows a slope that is more consistent with the data and has a reduced cash statistical value of 3.29. This lower value, as well as the smaller deviation observed in the residuals, indicate that the best fit model was a better fit for the soft region. After comparing the overall shape of each model, analysing the residuals and the reduced cash statistical values, the best fit model parameters seemed to be the obvious choice to form the foundation of the continuum model and use for the remainder of the fitting process.

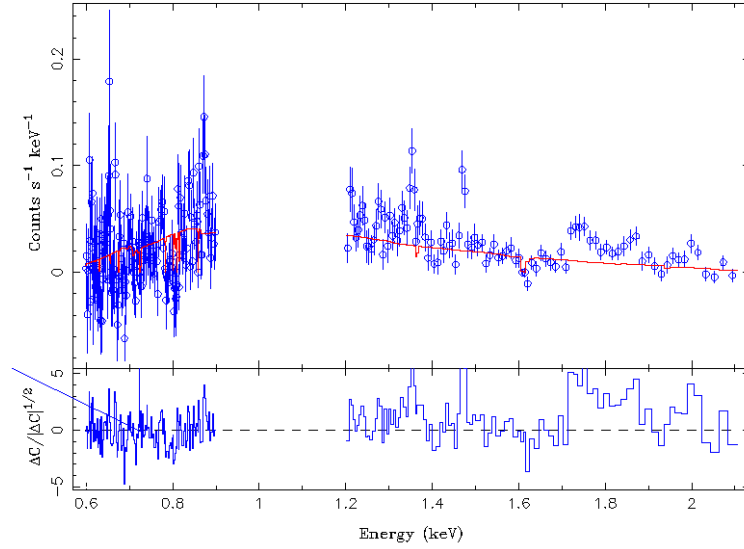
4.4.4 Narrow Band Spectral features

Having established the best fit values for absorption expressed through the equivalent hydrogen column density, $N_H = 0.76^{+0.04}_{-0.03}$, and the power law slope, $\Gamma = 2.9^{+0.3}_{-0.2}$, the parameters could be fixed and the next phase of the fitting process executed. As it was shown in section 5.1.5, see figure 4.8, below $\sim 2.6 \text{ keV}$ the spectrum is complex and portrays the potential existence of emission lines. This is more apparent in the highly resolved spectral data of RGS 1. Moreover, previous studies on Vela X-1 found that there is an abundance of narrow band features in the spectrum, corresponding to the resonant transitions of highly ionised ions and RRC (Lomaeva et al. 2020; Grinberg et al. 2017; Amato et al. 2021).

In this section, a conventional manual approach was employed to search for narrow band features, utilising knowledge of line/RRC energies. For each emission line detected, a Gaussian function was added to the continuum model and an XSPEC redden function added for RRC. Therefore the overall model, including the narrow-band com-



(a) First spectral fit



(b) Second spectral fit

Figure 4.10: Power law comparison. Top panel: Fixed EPIC parameter fit, Bottom panel: Free parameter fit

ponents is described by:

$$\begin{aligned}
 F(E) = & tbabs_1 \times [Norm_1 \times E^{-\Gamma} \\
 & + \sum_{i=1}^n Gaussian_i + \sum_{i=1}^m RRC_i]
 \end{aligned}
 \tag{4.8}$$

That is, one power law complemented by n Gaussian emission lines and m RRC, all being absorbed in the the material that has a column density N_H specified above.

During the fitting process, most Gaussian components were found to be really narrow and any changes made to the width of the Gaussian components did not improve the fit. For this reason the line widths were fixed and assumed to be zero. When the center energy of each line was determined, a cross check with laboratory energies was carried out to identify the lines. To optimise the line search, the spectrum was divided into four separate regions, following similar ranges outlined in Lomaeva et al. (2020). Figure 4.11 shows the different regions and their specified energy range: Top left: 0.6-0.8 keV, Top right: 0.8-0.9 keV, Bottom left: 1.2-1.6 keV and Bottom Right: 1.6-2.1 keV. The detected lines were identified as the following: **O VIII L α** , **Mg XI r**, **Mg XII L α** , **Si XIII r**, **Si XIV L α** , **Si II-VI K α** which is a blend of the K α lines from **Si II-VI**, and also **O VIII RRC**. For each line-like feature, the best fit parameters were determined using a 90% confidence interval to calculate the errors. The most likely identification of the line-like features along with the reference/detected energies and line flux are shown in table 4.2.

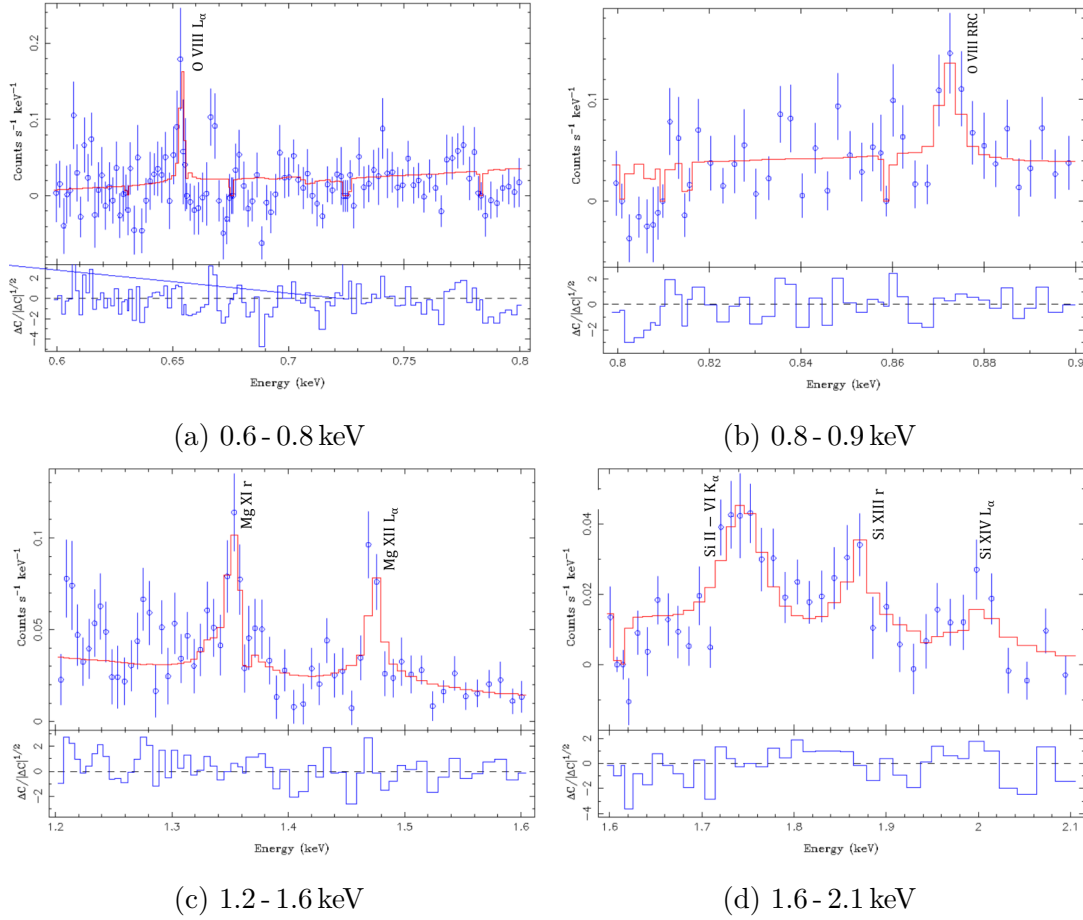


Figure 4.11: RGS

4.4.5 Radiative recombination continua

At $870.5^{+1.8}_{-0.8}$ eV a narrow band feature is observed in the spectrum. This was identified as **O VIII RRC**, which has a reference energy of 871.41 eV (Garcia & Mack 1965). The observed plasma temperature is $kT_p = 3.0^{+6.64}_{-1.5}$ eV, where k is the Boltzmann constant and has a value of $k = 8.6173 \times 10^{-5}$ eV K $^{-1}$. A simple calculation gives the temperature in Kelvins, which is on the order of $\sim 3.5 \times 10^4$ K. Lastly, the normalisation was determined to be $N = 12^{+18.2}_{-7.0}$ ph cm $^{-2}$ s $^{-1}$.

Table 4.2: Detected emission lines for RGS 1 spectrum

Line	Ion	Ref. Energy [eV]	Det. Energy [eV]	Line flux [ph s $^{-1}$ cm $^{-2}$ $\times 10^{-5}$]
O VIII L $_{\alpha}$	H-like	654.12 ^(a)	652.8 $^{+0.9}_{-0.7}$	28.4 $^{+40.1}_{-10.6}$
Mg XI r	He-like	1352.22 ^(a)	1352.8 $^{+3.0}_{-2.0}$	8.1 $^{+10.4}_{-6.5}$
Mg XII L $_{\alpha}$	H-like	1472.32 ^(b)	1470.9 $^{+2.8}_{-2.0}$	6.0 $^{+7.8}_{-4.5}$
Si II-VI K $_{\alpha}$	Al- to Na- like	1742.04 ^(a)	1753.1 $^{+9.0}_{-7.0}$	11.2 $^{+13.2}_{-9.0}$
Si XIII r	He-like	1864.10 ^(a)	1870.0 $^{+3.1}_{-21.7}$	5.4 $^{+9.3}_{-4.2}$
Si XIV L $_{\alpha}$	H-like	2005.67 ^(c)	2004.9 $^{+4.1}_{-16.7}$	7.4 $^{+10.9}_{-4.6}$

References: ^(a)Drake (1988), ^(b)Erickson (1977), ^(c)Garcia & Mack (1965)

4.4.6 Best Fit model

Figure 4.13 shows the best fit model for RGS 1 between 0.6 - 2.1 keV. All identified line-like features have been labelled and the corresponding parameters provided in table 4.2, whilst the RRC parameters are outlined in the previous section above. As the spectrum and axes have already been explained there is no need for a repeated explanation. Each feature in the spectrum was identified using the naked eye. Therefore, given the resolution of RGS 1 and the fact that the data exhibits a great deal of noise, only the features that strongly stood out against the background could be modelled successfully. The quality of fit is fairly decent, with some deviation observed in the residuals. The corresponding value for the reduced cash statistics is 1.85, however, a better fit is most likely achievable, which the parameters will be varied and thoroughly explored to flesh out any improvements when it comes to publishing the paper.

Examining the spectrum, the overall shape of the model is good, however, one section, particularly within the bounds of 1.2-1.3 keV, an inconsistency between the data and model is observed. A few emission lines have been detected in this region by Amato et al. (2021) using Chandra/HETGS data at a similar orbital phase of 0.75. Therefore an attempt to fit what appears to be possible line-like features was carried out, but with no success. After assessing the residuals, it became evident that the features were too narrow for ISIS to detect. For this reason, no fit could be made for such narrow features and, thus, up to the present date this is the best fit model that could be attained.

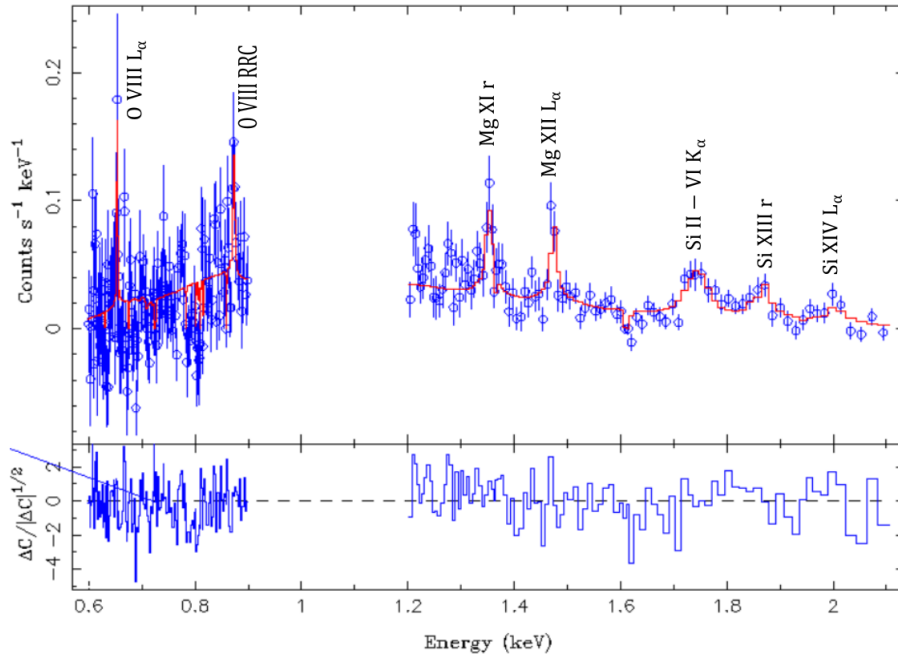


Figure 4.12: RGS 1 Best fit model

4.4.7 Model Comparison

Although an adequate model, with the best fit parameters acquired, it was still necessary to test the third power law component, to rule out any doubt of its inclusiveness. In this section a model independent of the power law was constructed and a comparison between both models implemented. Having already calculated the parameters for all the line-like features in the spectrum, the observed centroid energy for each emission line and RRC, see table 4.2, served as a baseline to guide the fitting process in this section, simplifying the whole procedure. The overall model with only absorbed narrow-band features and RRC is described by:

$$F(E) = tbabs_1 \times \left[\sum_{i=1}^n Gaussian_i + \sum_{i=1}^m RRC_i \right] \quad (4.9)$$

That is, n absorbed Gaussian emission lines and m absorbed RRC. Figure 4.10 shows the spectral fit of this model. It is immediately obvious that there is a large disparity between the data and model. This is further illustrated in the residuals and by the reduced cash statistical value being 6.86. This is much greater than 1.85 obtained from the previous best fit model, which indicates a terrible fit in comparison. Therefore, after assessing and comparing all the different models generated through out this entire section, the parameters obtained from equation 4.9, were determined as the most appropriate parameters to use for the analysis.

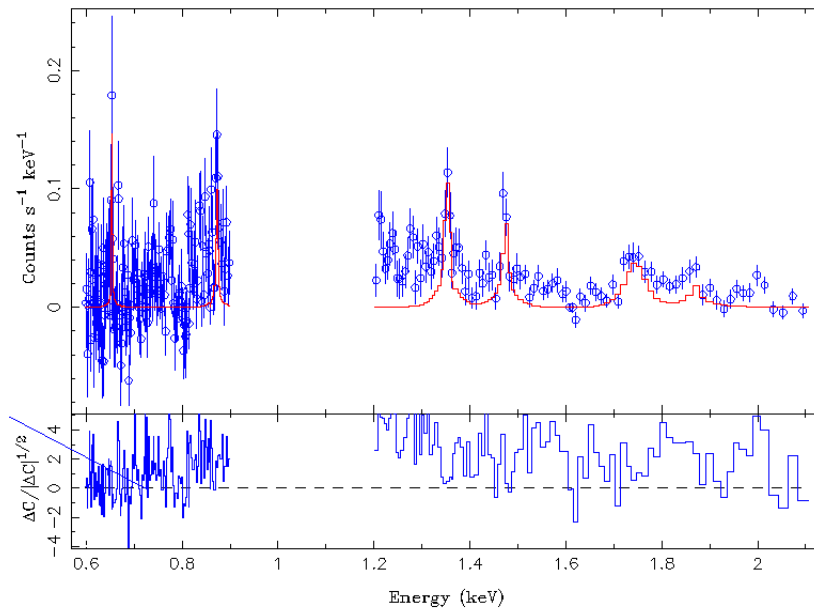


Figure 4.13: RGS 1 Best fit model

4.4.8 Line Velocities

Now that a suitable continuum model describing the soft X-ray emission of Vela X-1 had been successfully developed, the parameters derived were used to calculate the line velocities using equation 1.12. The equation is dependent on the observed wavelength of the emission lines and the measured wavelength in the laboratory, both of which are listed in table 4.3, along side the calculated velocities for each identified line. Here the centroid energies have been converted to wavelength and given in Angstrom. The velocity of most lines are consistent with zero, which is expected given the large uncertainties resulting from the resolution of the RGS detectors and the fact that the velocities are usually measured around a few hundred km/s. However, there were two

exceptions, the **O VIII L_α** and **Si II-VI K_α** lines, which will be elaborated on in the discussion & conclusion section.

Table 4.3: Line Velocities

Line	Ion	Ref.	Det.	Velocity
		Wavelength	Wavelength	
		[Å]	[Å]	[km s ⁻¹]
O VIII L _α	H-like	18.9544 ^(a)	18.97 ^{+0.02} _{-0.03}	598 ⁺³²⁴ ₋₄₀₅
Mg XI r	He-like	9.16896 ^(a)	9.17 ^{+0.01} _{-0.02}	-120 ⁺⁴³⁵ ₋₆₃₄
Mg XII L _α	H-like	8.42101 ^(b)	8.43 ^{+0.01} _{-0.02}	291 ⁺⁴⁰⁷ ₋₅₇₈
Si II-VI K _α	Al- to Na- like	7.1172 ^(a)	7.07 ^{+0.03} _{-0.04}	-1895 ⁺¹¹⁹¹ ₋₁₄₇₈
Si XIII r	He-like	6.64795 ^(a)	6.63 ^{+0.08} _{-0.01}	-821 ⁺³⁵⁸² ₋₄₉₈
Si XIV L _α	H-like	6.1817 ^(c)	6.18 ^{+0.05} _{-0.01}	114 ⁺²⁵¹³ ₋₆₁₈

References: ^(a)Drake (1988), ^(b)Erickson (1977), ^(c)Garcia & Mack (1965)

Discussion

This section is a discussion of the results obtained in the context of this work

5.1 Light Curves

Vela X-1 is known to have intense X-ray variability of varying lengths. For this observation the variation dealt with was on time scales above 1 pulse period, which in general is fairly stable. The light curves generated from the EPIC-pn data, show that variations in flux are observed overall and in different energy bands, see figures 4.1 and 4.2. The short-term variability, ~ 1 ks, is mostly driven by intrinsic flux variations from X-ray emission in the source, which is thought to be related to the changes in the accretion rate and inhomogeneities in the stellar wind flow (Haberl & White 1990; Nagase et al. 1983). Analysis on a larger time scale and in particular, between ≈ 15 ks and ≈ 20 ks, see figure 4.1, shows that the brightness increases from $\approx 60 \text{ cts s}^{-1}$ and peaks at $\approx 140 \text{ cts s}^{-1}$, which suggests the presence of a possible flare. Although this can not be conclusively shown, flares have been observed multiple times in Vela X-1, with flux sometimes increasing 10 fold above normal emission during active states (Martínez-Núñez et al. 2014). The accretion of clumpy wind material onto the NS surface has been proposed by numerous authors as a possible cause for bright flares (Kreykenbohm et al. 2008; Fürst et al. 2010; Martínez-Núñez et al. 2014), where as, Manousakis & Walter (2015) relate flares to unstable hydrodynamic flows.

5.2 Accretion structure

The model describing the X-ray emission of the EPIC-pn detector, follows the work carried out by Martínez-Núñez et al. (2014), and drives the interpretation of the spectra developed for both the EPIC and RGS observational data.

Martínez-Núñez et al. (2014) were able to obtain a good fit of the spectrum for Vela X-1 using three absorbed power laws with identical photon index, but different normalisation and column density. Two power laws were used to describe the hard region of the spectrum, where the behaviour of each component was traced during

the flare. Their results suggested that the first two components were two aspects of the same component that originated close to the neutron star surface. It is also explained in Kretschmar et al. (2019) that for X-ray binaries, Compton scattering of thermal seed photons in a hot and dense medium close to the compact object is the non-thermal process by which the power law-like spectra are made, where the slope and normalisation of the power law do not have a direct physical meaning (Grinberg et al. 2017).

As the photons that form the first two components in the spectrum pass through the extended stellar wind material, a portion experience Thomson scattering with free electrons in the ionised plasma. This interaction is more likely to occur with lower energy photons. The ionisation state of the plasma is indicated by the detection of highly ionised ions that generate emission lines in the spectrum of Vela X-1 for similar orbital phases as seen in other studies carried out by Lomaeva et al. (2020); Grinberg et al. (2017). During this process only the direction of the photons are changed, which the photons that are scattered into our line of sight form the additional third component that describes the soft region of their spectrum.

Adopting this interpretation and following the same strategy, the hard spectrum was successfully modelled using EPIC-pn observational data. This was achieved by summing two absorbed power law components and tying each photon index together. The best fit value was found to be $\Gamma=1.606^{+0.02}_{-0.003}$, which was very close to the value determined by Martínez-Núñez et al. (2014). Given that X-ray emission forming each component passed through different regions in the material, see figure 5.1, absorption for component 2, $N_H^{(2)} = 44.47^{+1.26}_{-1.12} \times 10^{22} \text{ cm}^{-2}$, was greater than component 1, $N_H^{(1)} = 13.46^{+2.26}_{-2.37} \times 10^{22} \text{ cm}^{-2}$. For this reason the **Fe K $_{\alpha}$** and **Fe K $_{\beta}$** fluorescence lines were associated with component 2, as this component passed through the more dense region, where it is assumed the majority of the iron atoms responsible for the emission lines are located. The **Fe K $_{\alpha}$** and **Fe K $_{\beta}$** were both successfully modelled, with center energy values that were close to the values determined in Martínez-Núñez et al. (2014). Results from Martínez-Núñez et al. (2014), also show the presence of the **Ni K $_{\alpha}$** line, however, this emission line could not be detected by a visual inspection or any trial fits attempted in the expected region during the analysis process.

The soft region was also modelled successfully owing to the analysis carried out using data from RGS 1 rather than the EPIC-pn detector, as this instrument provided better resolution. This made it possible to improve the parameters of the third component and determine if there was indeed an echo present in the wind and to further investigate the contribution from emission lines and RRC.

During the analysis, the absorption associated with the third component, expressed

as column density, was $N_H^{(3)} = 0.76_{-0.03}^{+0.04} \times 10^{22}$, which is consistent with the value determined by Martínez-Núñez et al. (2014). By trialing a number of different models, the third component was found to be an essential element of the spectrum. However, the value determined for the photon index was $\Gamma = 2.9_{-0.2}^{+0.3}$, which is inconsistent with the value determined by Martínez-Núñez et al. (2014). This result shows that the photon index for all three components are not identical and that the current interpretation may need revision. A physical explanation for this result is yet to be determined, but is currently in progress and will be provided in the paper.

Figure 5.1 is a schematic view of the interpretation for this observation. It shows X-ray emission from near the NS surface. The emitted X-rays pass through two different regions in the stellar wind material, which correspond to the first two power law components. The exponent is shown with a red background, which indicates that each photon index has identical values, as both power laws are two aspects of the same component. A portion of the first two components are scattered by free electrons in the wind, which form the third power law. The photon index for the third component has no coloured background because it has a different value to the first two components. Lastly each power law has an absorption model tied to them, which are displayed in figure 5.1. All the emission that come into our line of sight forms the spectral data we observe.

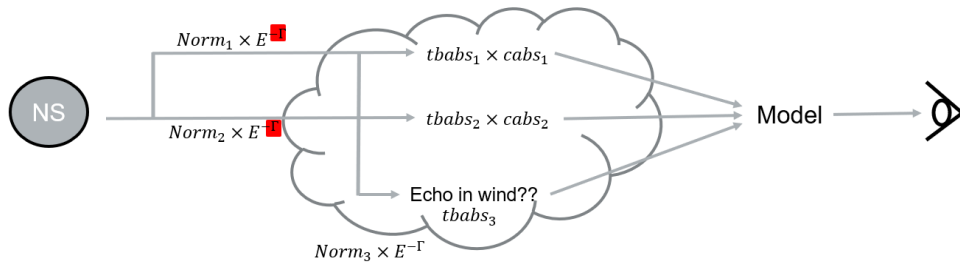


Figure 5.1: Schematic view of the physical interpretation

5.3 Narrow-band Spectral Features

The energy range covered by the RGS detectors has a high density of RRC and X-ray emission lines which include, K-shell transitions and **He**-like triplets of light elements, such as **C**, **N**, **O**, **Ne**, **Mg** and **Si**. There are also the L-shell transitions of heavier elements like **Fe** and **Ni**. Since data from only the RGS 1 detector was available, a gap in the spectrum is observed between $\sim 0.9 - 1.2$ keV, which is where important **Ne** lines are found. For example Lomaeva et al. (2020) found the **Ne XII** L_α triplet and **Ne X** L_α lines. The detection of **H** and **He**-like ions and RRC, enables the use of

a large number of diagnostic tools, to determine the physical conditions and chemical composition of the stellar wind material.

For this observation, the **O VIII L_α**, **Mg XI r**, **Mg XII L_α**, **Si XIII r**, **Si XIV L_α**, **Si II-VI K_α** emission lines, and also **O VIII RRC** were detected, see table 4.2 and section 5.2.6. This gives insight into the chemical composition of the stellar wind material, but also indicates that the plasma is photoionised. The temperature of the plasma was obtained from the RRC feature, see section 5.2.6, which the calculated value is on the order of $\sim 3.5 \times 10^4$ K, which is consistent with Lomaeva et al. (2020).

For each of the emission lines, the velocities were also calculated, where all but two features were consistent with zero, see table 4.3. The two exceptions were the **Si II-VI K_α** blend and the **O VIII L_α** line. Grinberg et al. (2017) explains how the properties of the plasma in the extended stellar wind determines the contribution of lines to the **Si II-VI K_α** blend, which differs to contributions found in a laboratory environment, where an Electron Beam Ion Trap (EBIT) is used to replicate cosmic plasma. Since differing environments play a role in the contribution to the narrow band features this can affect the measured center energy resulting in the presence of inaccurate theoretical reference values. Grinberg et al. (2017) also point out that laboratory values for silicon and sulfur from Hell et al. (2016) are inconsistent with calculations determined by Behar & Netzer (2002), such that velocities can differ by up to 300 km s^{-1} for lower ionization stages, which may extend to other detected ions such as **O VIII L_α**. This is most likely the cause for the inconsistent calculated line velocities for the two features in this work.

A further investigation of the plasma, can be obtained through R and G diagnostics. This procedure is still underway, but a short discussion about it and the next steps for the paper are included in the following section.

5.4 R and G diagnostic

There are two ratios that can be calculated from the normalisation of the forbidden (f), intercombination (i), and resonance (r) lines of He-like triplets. These are defined as $R=f/i$ and $G=(f+i)/r$, where R depends on electron density (n_e), where as G depends on electron temperature (T_e) and is independent of density. This is great because these ratios can be used to probe the temperature, density, and ionising process in the stellar wind structure of Vela X-1 (Gabriel & Jordan 1969; Porquet & Dubau 2000; Lomaeva et al. 2020). The idea is to fit three Gaussian functions for an observed triplet in order to estimate the parameters. That is the center line energy, width and intensity. The line intensity of the intercombination and resonance lines are then expressed as a factor

containing R and/or G according to the equations above, while the normalisation of the model corresponds to the line intensity of the forbidden line. This approach allows us to directly fit and constrain values for R and G and thus n_e and T_e of the plasma. This procedure will be included in the paper.

Conclusion

The XMM-Newton observation during orbital phases from $\phi_{orb} = 0.63 - 0.75$ has revealed new insight into the spectral model of the Vela X-1 system and potentially our understanding for the model interpretation. Particularly the photon index of the third power law component having different value to the first and second power law components. This is inconsistent with previous models, which a physical interpretation for the results in this work is currently in progress. Moreover, the necessity of the third component was confirmed, indicating that scattered emission by electrons (an echo) is occurring in the extended stellar wind material of HD 7758. In addition to these findings, a firm detection of highly ionised elements and RRC were shown to exist, indicating that the plasma is ionised. Furthermore the line velocities were shown to be consistent with zero. From the light curve analysis, strong variations were shown, overall and in the relative flux of different bands, for time scales above 1 pulse period, both short and long term variability, which showed the presence of a possible flare during the observation.

While these results may provide new insight into the stellar wind structure of Vela X-1, further analysis is needed and is currently underway. The work from the ongoing analysis will be available in the paper. Should the reader be interested, the paper will be submitted for peer review for the Astronomy and Astrophysics journal no later than the end of January 2022.

Title Appendix

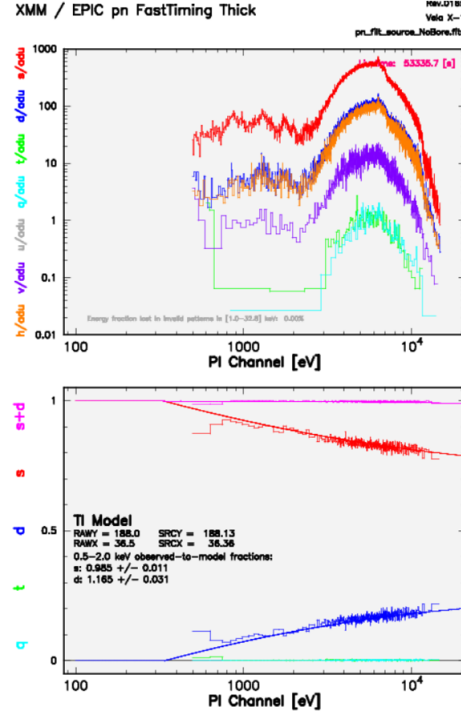


Figure 1: Two pixel columns either side of the boresight

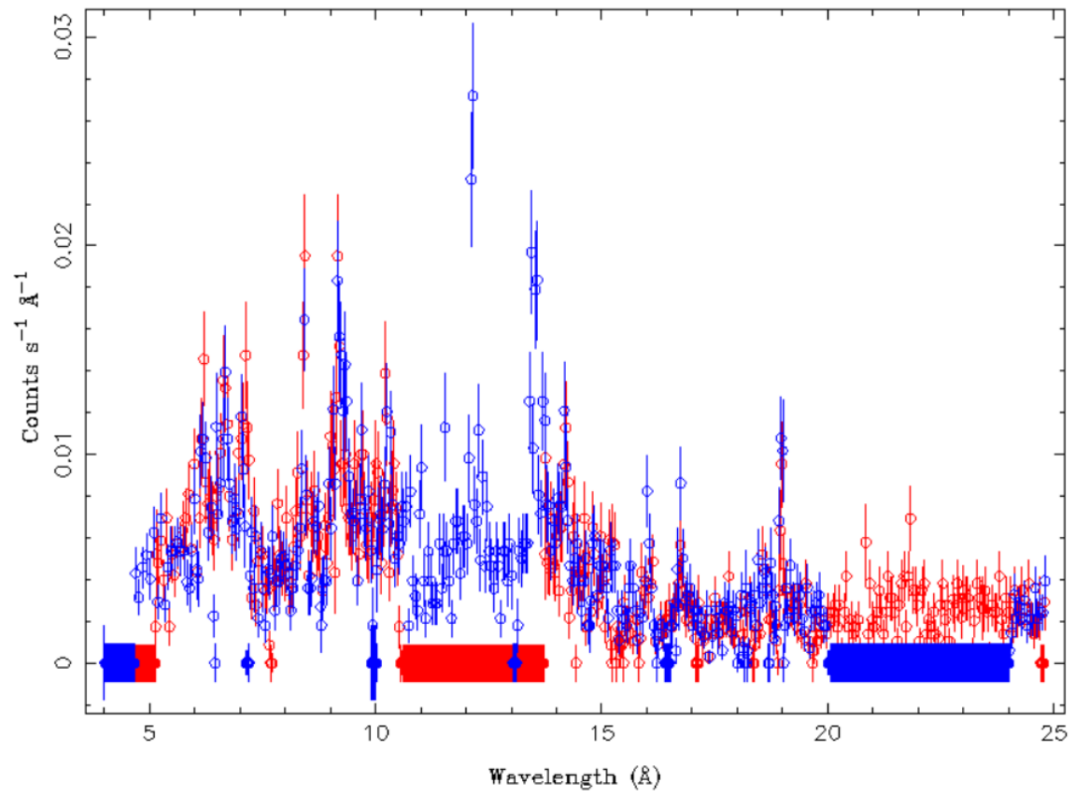


Figure 2: Groupings

Bibliography

- Amato, R., Grinberg, V., Hell, N., et al. 2021, A&A, 648
- Arnaud, K., Gordon, C., & Dorman, B. 2021, Xspec - An X-Ray Spectral Fitting Package, Users' Guide for version 12.12
- ASTRO-H CookBook Members. 2015, A First Step to ASTRO-H Spectral Analysis, rev 0.1
- Bailer-Jones, C. A. L., Rybizki, J., Fouesneau, M., Mantelet, G., & Andrae, R. 2018, AJ, 156, 58
- Basko, M. M. & Syunyayev, R. A. 1976, MNRAS, 175, 395
- Becker, P. A., Klochkov, D. Schönherr, G., Nishimura, O., et al. 2012, A&A, 544, 123
- Behar, E. & Netzer, H. 2002, ApJ, 570, 165
- Bildstenl, L., Chakrabarty, D., Chiu, J., et al. 1997, ApJSS, 113, 367
- Blondin, J. M., Kallman, T. R., Fryxell, B. A., et al. 1990, ApJ, 356, 591
- Casares, J., Jonker, P. G., & Israelian, G. 2017, Handbook of Supernovae, 1499
- Cash, W. 1979, ApJ, 228, 939
- Chodil, G., Mark, H., Rodrigues, R., Seward, F. D., & Swift, C. D. 1967, ApJ, 150, 57
- Courvoisier, T. J.-L. 2013, High Energy Astrophysics, 223
- den Herder, J. W., Brinkman, A. C., Kahn, S. M., et al. 2000, A&A
- Drake, G. W. 1988, Can. J. Phys, 66, 586
- Eisberg, R. & Resnick, R. 1985, Quantum Physics of Atoms, Molecules, Solids, Nuclei, and Particles, 2nd Ed.
- Erickson, G. W. 1977, J. Phys. Chem. Ref. Data, 6, 831
- ESA: XMM-Newton SOC. 2019, XMM-Newton Users Handbook, Issue 2.17
- Forman, W., Jones, C., Tananbaum, H., et al. 1973, ApJ, 182, L103
- Fürst, F., Kreykenbohm, I., Pottschmidt, K., et al. 2010, A&A, 519, A37
- Gabriel, A. H. & Jordan, C. 1969, MNRAS, 145, 241
- Garcia, J. D. & Mack, J. E. 1965, Journal of the Optical Society of America (1917-1983), 55, 654
- George, I. M., Arnaud, K. A., Pence, B., Ruamsuwan, L., & Corcoran, M. F. 2007, The Calibration Requirements for Spectral Analysis, Technical report, NASA/GSFC

- Giménez-García, A., Shenar, T., Torrenjón, J. M., Oskinova, L., & Martínez-Núñez, S. 2016, *A&A*, 591, A26
- Grinberg, V., Hell, N., El Mellah, I., Neilsen, J., et al. 2017, *A&A*, 608, A143
- Haberl, F. & White, N. E. 1990, *ApJ*, 361, 225
- HEASARC. 2021, <https://heasarc.gsfc.nasa.gov/db-perl/W3Browse/w3table.pl#>
- Hell, N., Brown, G. V., Jörn, W., et al. 2016, *ApJ*, 830, 26
- Kaastra, J. S. & Bleeker, J. A. 2016, *A&A*, 587, 151
- Kaper, L., Hammerschlag-Hensberge, G., & Zuiderwijk, E. J. 1994, *A&A*, 289, 846
- Kretschmar, I., El Mellah, I., Martínez-Núñez, S., et al. 2021, *A&A*, 50
- Kretschmar, P., Fürst, F., Sidoli, L., et al. 2019, *New Astronomy Reviews*, 86, 61
- Kreykenbohm, I., Kretschmar, P., Wilms, J., et al. 1999, *A&A*, 341, 141
- Kreykenbohm, I., Wilms, J., Kretschmar, P., et al. 2008, *A&A*, 492, 511
- Lomaeva, M., Grinberg, V., Guainazzi, M., et al. 2020, , 641, A144
- Longair, M. S. 2011, *High Energy Astrophysics*
- Malacaria, C., Mihara, T., Santangelo, A., et al. 2016, *A&A*, 588, A100
- Manousakis, A. & Walter, R. 2015, *A&A*, 575, A58
- Martínez-Núñez, S., Torrejón, J. M., Kühnel, M., et al. 2014, *A&A*, 563, A70
- McClintock, J. E., Rappaport, S., Joss, P. C., et al. 1976, *ApJ*, 206, L99
- Mészáros, P. 1984, *SSR*, 38, 325
- Nagase, F., Hayakawa, S., Makino, F., Sato, N., & Makishima, K. 1983, *PASJ*, 25, 47
- Nagase, F., Hayakawa, S., Sato, N., Masai, K., & Inoue, H. 1986, *PASJ*, 38, 547
- Nowak, M. 2020, *Data Analysis with the Interactive Spectral Interpretation System*
- Odaka, H., Khangulyan, D., Tanaka, Y. T., et al. 2013, *ApJ*, 767, 70
- Porquet, D. & Dubau, J. 2000, *AAS*, 143, 495
- Press, W. H., Teukolsky, S. A., Vetterling, T. V., & Flannery, B. P. 1992, *Numerical Recipes in C - The Art of Scientific Computing*, 2nd Ed. (Cambridge University Press, New York, 1992)
- Quaintrell, H., Norton, A. J., Ash, T. D. C., et al. 2003, *A&A*, 401, 313
- Sander, A. A. C., Fürst, F., Kretschmar, P., et al. 2018, *A&A*, 610, A60
- Santangelo, A. 2021a, *Lecture in High Energy Astrophysics*
- Santangelo, A. 2021b, *Lecture in Extragalactic Astrophysics*
- Santangelo, A. & Grinberg, V. 2021, *Lecture in Astronomy and Astrophysics*
- Schönherr, G., Wilms, J., Kretschmar, P., Kreykenbohm, I., et al. 2007, *A&A*, 472, 353
- Sidoli, L., Paizis, A., Fürst, F., et al. 2015, *MNRAS*, 447, 1299
- Ulmer, M. P., Baity, W. A., Wheaton, W. A., & Peterson, L. E. 1972, *ApJ*, 178, 121

- van Loon, J. T., Kaper, L., & Hammerschlag-Hensberge, G. 2001, *A&A*, 375, 498
- Wilms, J. & Allen, A. McCray, R. 2000, *ApJ*, 542, 914
- Yuichiro, E., Takaya, O., & Kazuhisa, M. 2021, *Rev. Mod. Plasma Phys.*, 5, 4

Acknowledgements

I would like to thank all those who contributed to the work involved in this thesis. This would not have been possible without your help and I would like to dedicate this acknowledgment to the main contributors. Prof. Dott. Andrea Santangelo, thank you for allowing me to join your group and providing me with an opportunity to do an exciting project where I could gain experience in scientific research. I would also like to thank you for providing me with a Hiwi contract to publish a paper from the research involved in this thesis work. This means a lot to me and I can not express how grateful I am for this. In addition to the opportunities you have provided I would also like to thank you for proof reading the thesis. Dr. Victoria Grinberg, I can not thank you enough for your supervision. The kindness and patience you showed as a supervisor was nothing short of amazing. You have been the biggest help and guidance. I couldn't have asked for a better mentor. I am really lucky to have worked with you personally. You showed humility and care for everyone in your group. Your knowledge, experience, work ethic and professionalism showed me what it takes to be a great scientist and has inspired me and reinforced my desire to pursue my career in Astrophysics. Thank you so much you are the best. Lastly I'd like to give a quick shout out to my friend Stephen Walker (LSF) for his support.